RSC Advances

PAPER

View Article Online
View Journal | View Issue

Cite this: *RSC Adv.*, 2025, **15**, 46277

Novel NiCoMn–PDC MOFs: a dual-functional material for electrocatalytic water splitting and hybrid supercapacitor applications

Sharif Ullah,†[a] Khurram Imran Khan, †*[a] Muhammad Ramzan Abdul Karim †*[a] and Anique Ahmed†[b]

Addressing the global energy crisis needs advanced materials capable of both high-capacity energy storage and efficient electrocatalytic water splitting. Current technologies face challenges related to the low energy density of supercapacitors and sluggish reaction kinetics of the hydrogen evolution reaction and oxygen evolution reaction in water splitting. We hydrothermally synthesized a novel ternary Ni–Co–Mn metal–organic framework using 2,6-pyridine dicarboxylic acid as the organic ligand. As an electrocatalyst, the material achieves lower overpotentials of 47 mV for the hydrogen evolution reaction and 61 mV for the oxygen evolution reaction at a current density of 10 mA cm^{-2}, along with a Tafel slope of 60 mV dec^{-1}. For energy storage, it delivers specific capacitances of 1070 F g^{-1} (CV, 2 mV s^{-1}) and 840 F g^{-1} (GCD, 0.5 A g^{-1}) as well as a specific capacity of 420 C g^{-1}. The fabricated hybrid supercapacitor device exhibits a power density of 475 W kg^{-1} and an energy density of 45 Wh kg^{-1}. Moreover, it showed a coulombic efficiency of 99.88% and stability of 79.01% after 5000 charge–discharge cycles. This work introduces a successful material design strategy by integrating high-capacity charge storage and superior electrocatalysis within a single MOF framework.

Received 3rd August 2025
Accepted 29th October 2025

DOI: 10.1039/d5ra05650k

rsc.li/rsc-advances

1. Introduction

The escalating global energy crisis, which was previously met through fossil fuels, has triggered severe environmental degradation and gradual resource depletion.[1,2] Sustainable alternatives like solar and wind energy offer minimal or no carbon footprints but suffer from inherent intermittency.[3] Solar irradiation is limited to daylight hours and wind patterns fluctuate seasonally, creating significant gaps in energy storage.[4,5] Therefore, this underscores the urgent need for integrated systems capable of both efficient energy storage and on-demand production at basic and technological levels.[6–8] Among multiple emerging solutions, electrocatalytic water splitting represents a transformative solution.[9] Electrocatalytic water splitting utilizes renewable electricity to split water and produces hydrogen, a facile energy carrier.[10–12] However, this process is impeded by the kinetically sluggish, four-electron oxygen evolution reaction (OER), alongside the two-electron hydrogen evolution reaction (HER).[13,14] As such, the OER is considered a performance-limiting factor for the water-splitting reaction.[15–17] Therefore, a catalyst must be developed that significantly improves the reaction mechanisms by overcoming the sluggish kinetics. While noble metals like ruthenium (Ru), iridium (Ir) and platinum (Pt) are benchmark catalysts and play important roles in significantly improving the electrocatalyst efficiency, their limited availability and high cost hinder their scalability.[18,19] Considering these aspects, it is increasingly important to further investigate alternative transition metal-based electrocatalysts that are cost-effective, more readily available, environmentally friendly, and demonstrate high stability and activity.[20,21] Transition metal-based materials are at the forefront of today's research, showing outstanding performance in terms of the HER and OER.[22]

Effectively tackling the intermittency of renewable energy sources requires high-performance energy storage beyond efficient energy production. A perpetual desire for energy storage has provoked significant research in the field of supercapacitors due to their remarkable advantages.[23] The benefits include exceptional cyclic stability, fast charge and discharge capabilities, and superior power density in comparison with secondary batteries.[24,25] Supercapacitors have extensive applications in portable electronic devices, power backup, and electric vehicles because of their higher power density.[23,26,27] However, supercapacitors undoubtedly show superior power density, but are limited by a comparatively lower energy density when compared to batteries and fuel cells.[28–30] According to the energy storage process, an electrochemical supercapacitor classified as an

[a]*Faculty of Materials and Chemical Engineering, Ghulam Ishaq Khan Institute of Engineering Sciences and Technology, Topi, 23640, Khyber Pakhtunkhwa, Pakistan. E-mail: khurram@giki.edu.pk; ramzan1109@hotmail.com; ramzan.karim@giki.edu.pk*

[b]*Faculty of Engineering Sciences, Ghulam Ishaq Khan Institute of Engineering Sciences and Technology, Topi, 23640, Khyber Pakhtunkhwa, Pakistan*

† All authors contributed equally.

electrical double-layer capacitor (EDLC) uses a carbon-based material that stores energy at the interface of the electrode and electrolyte through a non-faradaic process.[31,32] Subsequently, pseudo capacitors (PCs) utilize faradaic mechanisms for charge storage because they are based on metals that cause redox reactions.[33,34] On the other hand, a hybrid supercapacitor uses both faradaic and non-faradic mechanisms for charge storage.[35,36] Advanced supercapacitors with high energy density (E) and uncompromised power density (P) are essential for future energy storage needs. Their energy density depends on specific capacitance and the potential window.[37] To store energy in a supercapacitor at high voltage without compromising the specific capacitance, the exploration of new electrode materials is required.[38] Among various material options, transition metal-based electrodes are promising for supercapacitors due to their abundance, eco-friendliness, stability, electrochemical performance, and cost-effectiveness.[39]

The transition metal-based metal organic framework is considered the premier electrode material, which uniquely addresses two critical technologies: electrocatalytic water splitting and supercapacitors.[40,41] MOFs belong to the class of highly porous crystalline hybrid materials, which are formed by linking metal nodes with organic linkers through coordination bonds to create rigid, modular frameworks.[42–44] Their superiority stems from the atomic-level tunability of redox-active sites, high surface area, and nano-porosity that not only enables high-capacity energy storage, but also electrocatalytic HER/OER kinetics.[45,46] The unique architecture of MOFs offers advantages, allowing them to serve as attractive solutions for various applications across multiple fields, including electrocatalytic water splitting, energy storage, gas separation, sensing, and absorption.[47] The customizable microstructure exhibited by MOFs attained *via* synthesis techniques helps in the precise control of their porosity.[48] The obtained MOF crystal displays open and extensive porous channels, extending over several microns. The porous cavity serves an essential function as a reservoir for cations and anions during the GCD charge–discharge process when employed as an electrode material in a supercapacitor.[49] Similarly, porous cavities play crucial roles during the redox process in the HER and OER when used as electrocatalysts for electrocatalytic water splitting processes.[49–51] The unique characteristics of this porous cavity facilitate ion retention and diffusion, leading to enhanced electrochemical efficiency for supercapacitors and electrocatalytic water splitting.[52,53] The selection of organic linkers is pivotal to the modulation of MOF properties; pyridine dicarboxylate (PDC) is particularly appealing due to its geometrically flexible yet rigid coordination, allowing for the synthesis of stable MOFs with modulable electrochemical activity.[53] Monometallic MOFs (*i.e.*, CO-ZIF-67) are simple to synthesize and exhibit uniform active sites but suffer from limited active site availability, restricted redox chemistry, and poor conductivity, which result in lower energy storage capacities in supercapacitors as well as increased catalytic overpotential in electrocatalytic water splitting. In many cases, monometallic MOFs cannot exhibit ideal behavior in electrochemical applications. Bimetallic MOFs (*i.e.*, Ni–Co–HMT) involve the incorporation of two metals in the framework during synthesis, resulting in superior performance when compared to monometallic MOFs, owing to the improved conductivity and the introduction of dual redox activity through charge transfer between heteroatoms.[54] Bimetallic catalysts still face some limitations, such as insufficient active site tunability in cases of complex reactions (*i.e.*, simultaneously for HER/OER) and sluggish kinetics in multi-electron transfer processes.[55] In contrast, ternary MOFs show a paradigm shift in the material design through synergistic multifunctionality by overcoming the fundamental limitation of mono- and bi-metallic MOFs.[56] Ternary MOFs (*i.e.*, Ni–Co–Mn–TPA), which feature three different metals, not only stabilize redox reactions, enabling electron transfer for ultrahigh specific capacitance in hybrid supercapacitors, but also expose abundantly unsaturated active sites that accelerate reaction kinetics by lowering the overpotential in the case of electrocatalytic water splitting.[57] The ability of the ternary system not only avoids disorder phases through precisely controlled synthesis, but also integrates the complementary functionality of different transition metals like the conductivity of nickel, oxygen affinity of cobalt, and structural stability of manganese within the single crystalline framework.

Leveraging the promise of these transition metal-based frameworks, we focus here on nickel, cobalt, and manganese to exploit their potential for electrocatalytic water splitting and supercapacitor applications. Nickel MOFs are highly efficient among transition metal-based MOFs, owing to nickel's natural conductivity, earth abundance, cost-effectiveness, electrocatalytic properties, and strong energy storage capacity.[40] In this case study, Khan *et al.*[58] synthesized Ni–Mn MOF, exhibiting excellent bifunctional performance with low OER (407 mV) and HER (196 mV) overpotentials at 10 mA cm^{-2}. Furthermore, in supercapacitors, the reversible (Ni^{2+} to Ni^{3+}) transition enables long cycling stability and outstanding pseudocapacitance (789 F g^{-1} at 1 A g^{-1}). Such dual functionality renders Ni-based MOFs economical alternatives for renewable energy systems. Similarly, cobalt MOFs also excel in both supercapacitor and electrocatalytic water splitting because cobalt atoms show a natural shift in oxidation from Co^{2+} to Co^{3+}, which enables efficient energy storage through rapid electron transfer.[59] Additionally, the cobalt MOFs porous structure creates vast amounts of surface area packed with active cobalt sites that easily interact with water molecules and speed up the HER and OER for hydrogen and oxygen evolutions, respectively. Khan *et al.*[60] synthesized Co-MOF using 2,6-pyridine dicarboxylic acid as a ligand, demonstrating exceptional catalytic performance with overpotentials of 180 mV for the oxygen (O_2) evolution reaction mechanism (OER) and 151.7 mV for the hydrogen (H_2) evolution reaction (HER) mechanism, respectively. In energy storage, Marwat *et al.*[1] synthesized nickel cobalt manganese and silver citrate-based MOFs through a solvothermal approach, demonstrating an excellent energy density of 61 Wh kg^{-1}, an ultra-high specific capacity of 762 C g^{-1}, and remarkable cyclic stability of 101% after 4000 cycles.

In this work, we hydrothermally synthesized ternary Ni–Co–Mn–PDC MOFs by integrating metal centers of nickel, cobalt, and manganese within the 2,6-pyridine dicarboxylic acid linker.

The fabricated materials were analyzed using physical characterization techniques, including (SEM) for morphology, (XRD) for crystallinity, (EDX) for elemental composition, and (FTIR) for identifying functional groups. To investigate the electrochemical properties, we constructed both two- and three-electrode assemblies. This material achieved an overpotential of 47 mV for (HER) and 60 mV for (OER) at a current density of 10 mA cm^{-2} with a Tafel slope of 60 mV dec^{-1}, which rivals that of noble metal benchmarks. For energy storage, it delivered a specific capacitance of 840 F g^{-1} at 0.5 A g^{-1} and a specific capacity of 420 C g^{-1}. The hybrid device (Ni–Co–Mn–PDC MOF||AC) exhibited an energy density of 45 Wh kg^{-1} and power density of 475 W kg^{-1} with 99.8% coulombic efficiency after 5000 cycles. The synergistic effect of Ni, Co, and Mn within the 2,6-pyridine dicarboxylic acid framework overcomes the sluggish OER/HER kinetics, thereby boosting the supercapacitor energy density.

2. Methodology

2.1 Chemicals

All chemicals were employed as obtained (purity ≥ 99.99%, Sigma-Aldrich & Alfa Aesar) without further purification: nickel(II) nitrate in hexahydrate crystalline form ($Ni(NO_3)_2 \cdot 6H_2O$), manganese(II) nitrate with variable hydration ($Mn(NO_3)_2 \cdot xH_2O$), and cobalt(II) nitrate with six coordinated water molecules ($Co(NO_3)_2 \cdot 6H_2O$) as the metal precursors, while pyridine-2,5-dicarboxylic acid (PDC) was used as the organic linker to synthesize the trimetallic MOF. *N*-Methyl-2-pyrrolidone (NMP) and ethanol were used as solvents, and deionized (DI) water was used throughout the synthesis. Acetylene black (conductive additive), polyvinylidene fluoride (binder, PVDF), and activated carbon or carbon black (AC) were used for the fabrication of the electrode, in addition to nickel foam (NF) as the current collector. Potassium hydroxide (KOH) pellets were dissolved in DI water to create the (1 M KOH) solution of alkaline electrolyte.

Table 1 Ratio optimization of Mn within S_1–S_4 MOFs

MOF	Name	Mn (%)	Ni (g)	Co (g)	Mn (g)	PDC (g)
$NiCoMn_{0.25}$–PDC	S_1	25	1.78	1.70	0.28	1
$NiCoMn_{0.05}$–PDC	S_2	5	1.78	1.70	0.05	1
$NiCoMn_{0.75}$–PDC	S_3	75	1.78	1.70	0.84	1
$NiCoMn_1$–PDC	S_4	100	1.78	1.70	1.13	1

2.2 MOF synthesis

The trimetallic Ni–Co–Mn-MOF was prepared with the help of the hydrothermal method, through systematic optimization of Ni–Co–Mn–PDC MOFs with high metal stoichiometric accuracy (S_1–S_4) (Fig. 1 and Table 1). The first step is the preparation of the precursor solution, in which the organic linker pyridine-2,5-dicarboxylic acid (PDC, 1 g) is dissolved in a mixed solvent (10 mL H_2O, 5 mL ethanol, 2.5 mL DMF) under stirring (30 min) to prepare solution A. Then, solution B is obtained by dissolving a stoichiometric amount of $Mn(NO_3)_2 \cdot xH_2O$ (0.28 g), $Ni(NO_3)_2 \cdot 6H_2O$ (1.78 g), and $Co(NO_3)_2 \cdot 6H_2O$ (1.70 g) in 15 mL DI water (30 min stirring). Following the precursor preparation, both solutions were mixed for 1 hour and then ultrasonicated for 20 minutes. They were subsequently hydrothermally treated within a Teflon-lined autoclave for 24 hours at 180 °C. The product was cooled, centrifuged, sequentially washed with ethyl alcohol, acetone, and deionized (DI) water, and then dried at 70 °C for 12 hours in a laboratory oven to achieve the final MOF powder sample. Furthermore, the compositional tuning maintained the fixed ratios of the organic linker (PDC), nickel, and cobalt (PDC : Ni : Co = 1 : 1.78 : 1.70) with variation in the Mn content (0.25–1.13 g) in compositions S_1–S_4. The reproducible method gives atomic-level control of Mn incorporation without losing crystallinity. The approach provides a roadmap for tailoring ternary metal–organic frameworks (MOFs) with customized redox properties for energy applications. While this study focused on tuning the Mn content, future investigations on varying Ni and Co ratios could further elucidate their

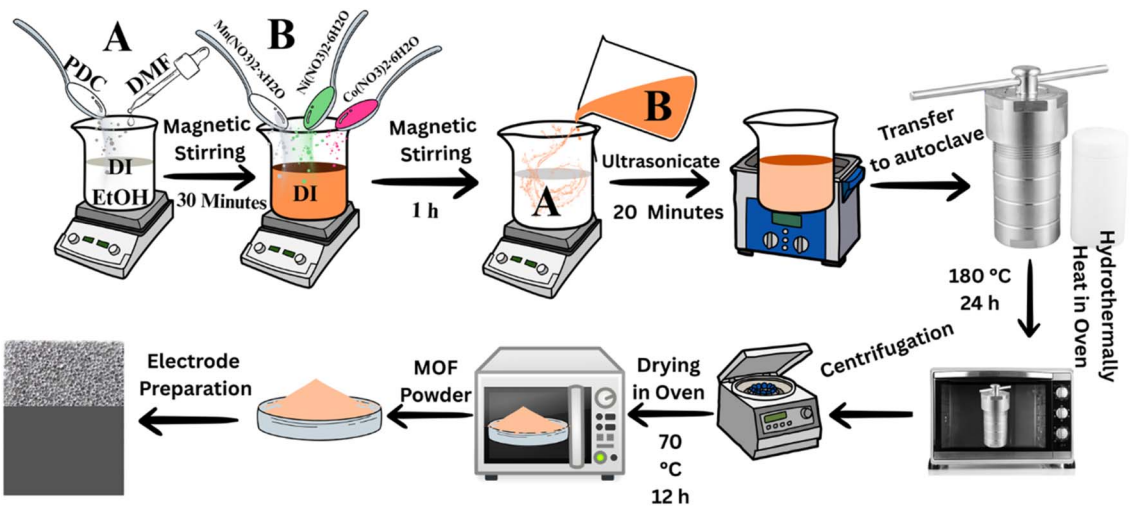

Fig. 1 Schematic of the hydrothermal method used to prepare S_1, S_2, S_3 and S_4 MOF compositions.

individual and synergistic contributions to the performance of ternary MOFs.

2.3 Electrode preparation

Nickel foam (1×1 cm^2) substrates were sequentially pretreated in 3 M HCl, ethanol, and acetone to erase surface oxides and organic contamination, and then thermally dried at 60 °C. The slurry was prepared by mixing the following components in an 80 : 10 : 10 wt% ratio of NiCoMn–PDC MOF powder, acetylene(carbon) black, and poly-vinylidene fluoride (PVDF, a binder) in a solvent of 1-methyl-2-pyrrolidone (NMP), with intensive magnetic agitation for 8 hours to maintain colloidal uniformity. The final slurry was deposited on pre-cleaned nickel foam substrates, and then dried out at 70 °C for 8 hours to produce working electrodes.

2.4 Material characterization

We characterized the prepared Ni–Co–Mn–PDC MOF by applying a scanning electron microscopy system (SEM, ZEISS EVO, UK), operating at 15 kV, to analyze its surface morphology. Subsequently, the elemental composition was validated through energy (E) dispersive X-ray spectroscopy analysis (EDX). Furthermore, the structural properties of the synthesized MOFs were characterized through X-ray diffraction (XRD) using a diffractometer (AXRD LPD, proto, UK) equipped with a copper Kα radiation source ($\lambda = 1.5418$ Å). The data were acquired over a continuous 2θ angular range of 5° to 80° as the equipment operated in θ–2θ configuration. During scanning, the diffraction angle (2θ) was incrementally increased while recording the X-ray diffraction intensity at each angular position, generating intensity *vs.* angle profiles that characterize the structural features of the samples. Likewise, identifications of the chemical bonding arrangements and functional groups were examined by Fourier (F) transform infrared spectroscopy (FTIR), spanning the mid-infrared range (400–4000 cm^{-1}), to confirm molecular coordination in the MOF structure. This study used a potentiostat (Galvanostat, Gamry Instruments, Reference 3000, United States) to assess the electrochemical performance in energy storage and water-splitting applications. This analysis includes methods such as linear sweep voltammetry (LSV), assessment of device cyclic stability, galvanostatic charge–discharge (GCD) and cyclic voltammetry (CV). A three-electrode (3E) configuration was employed, utilizing Hg/HgO as the reference electrode, a platinum (Pt) wire as the counter electrode, and a nickel foam as the substrate drop-cast with the active MOF material as the working electrode.

2.5 Electrochemical analysis

2.5.1 Water splitting analysis. We studied the performance of the synthesized electrode for the (HER) and (OER) in a typical three-electrode (3E) system by applying a potentiostat (Gamry Instrument, Reference 3000, United States). The catalyst material was utilized as the working electrode, while a typical Hg/HgO electrode served as the reference electrode and a platinum wire functioned as the counter electrode. All experiments were conducted in a one molar (1 M) KOH electrolyte solution. Linear sweep voltammetry (LSV) was performed at 5 mV s^{-1}, from 0 to −1.5 V for the hydrogen evolution reaction (HER) and from 0 to 1 V for the oxygen evolution reaction, with the potential measured relative to the reversible hydrogen (H) electrode (RHE). In this assessment, all potentials transformed into potential relatives to the reversible hydrogen electrode (RHE) using eqn (1), which is the Nernst equation.[61]

$$E(\mathrm{RHE}) = E_{\mathrm{Hg/HgO}} + E_0 + 0.059 \times \mathrm{PH} \quad (1)$$

We used impedance spectroscopy (EIS) to examine the resistance in charge transfer with a 5 mV AC amplitude over a frequency-spectrum range of (0.1 Hz to 100 kHz).

The ECSA was calculated from the double-layer capacitance (Cdl) measured through cyclic voltammetry (CV) conducted at various scan rates. A plot of the non-faradic current density (Δj) at 0.05 potential against the scan sweeps was made, and the slope provided the Cdl used for estimating the electrochemical surface area. The stability of the material was evaluated through chronopotentiometry or frequent cycles of cyclic voltammetry.

2.5.2 Energy storage analysis. The electrochemical (galvanic) analysis of NiCoMn-MOF was executed applying a potentiostat (Gamry Instruments, Reference 3000, United States) in a three-electrode (3E) assembly in 1 M KOH. This three-electrode (3E) configuration included Pt wire as the counter electrode, (Hg/HgO) as the reference electrode, and MOFs composition (S_1–S_4) as the working electrode. Three approaches were utilized for electrochemical investigations: galvanostatic charge–discharge (GCD) at 0.5 and 10 A g^{-1}, cyclic voltammetry (CV) swept from 5 to 100 mV s^{-1}, and impedance spectroscopy (EIS) from 0.1 Hz to 100 kHz. The specific capacitance (C_s) of the electrode was calculated from cyclic voltammograms using the formula presented in eqn (2).[62]

$$C_s = \frac{\int_{V_i}^{V_f} I \times dV}{m \times v \times \Delta V} \quad (2)$$

The symbol (V) represents the potential scan rate, which is quantified in millivolts per second (mV s^{-1}). The small (m) denotes the mass of the active material measured in grams, C_s signifies the specific capacitance expressed in (F g^{-1}), and the integral function illustrates the area (m^2) under the CV curve. The discharge curves facilitate the calculation of the specific capacity through eqn (3).[63]

$$Q_s = \frac{(I \times \Delta t)}{m} \quad (3)$$

In this context, Δt represents the discharge time, m denotes the electrode material mass, and I indicates the current. Similarly, eqn (4) was applied to find out the specific capacitance from the GCD curve.[64]

$$C_s = \frac{Q_s}{\Delta V} \quad (4)$$

Eqn (5) and (6) were used to find out the power density and energy density of the device, expressed in (W kg^{-1}) and (Wh kg^{-1}), respectively.[65]

$$P = \frac{3600 \times E}{\Delta t} \quad (5)$$

$$E = \frac{C_s \times V^2}{3.6 \times 2} \quad (6)$$

here, V represents the operational voltage, while Δt denotes the duration of discharge. They both assess how the material performs at the device level.

3. Results and discussion

3.1 Structural and morphological characterization

3.1.1 XRD analysis. The phase purity and crystallinity of the hydrothermally synthesized NiCoMn–PDC MOF were evidenced by X-ray diffraction (XRD), which showed peaks at 6.5°, 9.8°, 11.2°, 14.6°, 16.4°, 18.5°, 22.9°, 26.2°, 27.1°, and 30.5° (Fig. 2(a)). The NiO displayed characteristic peaks at 18.56° (102), 20.32° (112), 22.98° (013), and 26.25° (311). These peaks were matched by the literature, corresponding to JCPDS No. 25-0901.[66] Meanwhile, cobalt displayed intense reflections at 11.1° (100), 16.4° (010), and 27.1° (210), which matched with the literature, corresponding to JCPDS No. 43-1003.[60] The contributions of manganese were found at 6.5° (509), 14.6° (161), and 30.5° (111), which have the high-crystallinity sharp peak profiles confirmed by the literature pattern.[67] These peaks confirm the coexistence of Co, Mn and Ni oxide/hydroxide phases within the MOF framework.

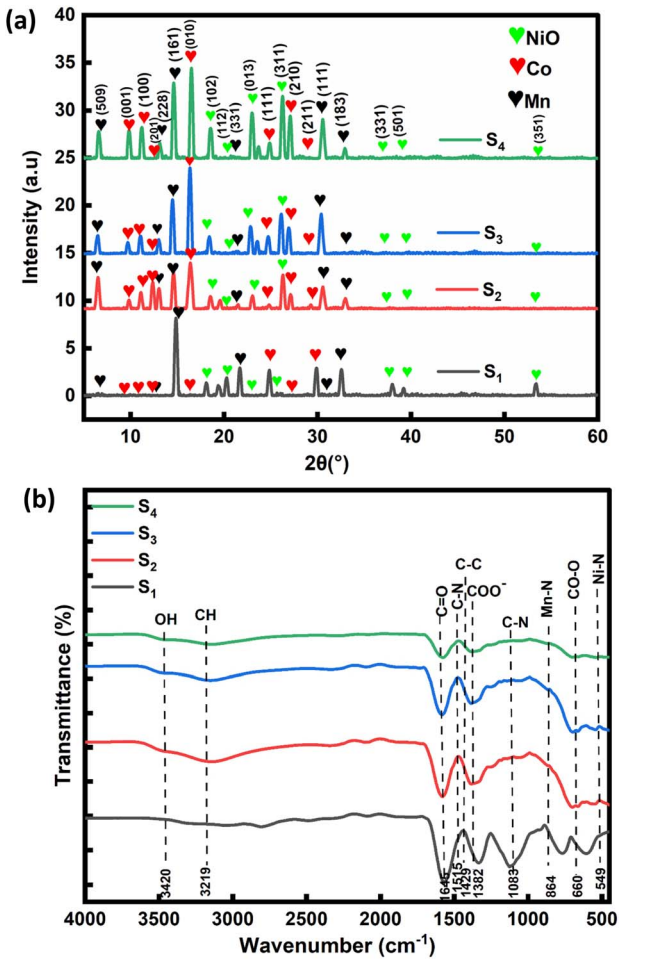

Fig. 2 (a) XRD patterns of the as-prepared trimetallic MOFs. (b) FTIR spectra of the trimetallic MOFs.

3.1.2 FTIR analysis. The FTIR spectra of the hydrothermally prepared Ni–Co–Mn–PDC MOF (Fig. 2(b)) shows characteristic vibrations that confirm the successful coordination of the 2,6-pyridine dicarboxylic acid ligand with metal ions. The FTIR spectra revealed a metal–ligand bonding environment, in which peaks were identified for carboxylate (COO^-) at 1382 cm^{-1}, O–H at 3420 cm^{-1}, C–H at 3219, C=O at 1645 cm^{-1}, and pyridinic (C–C/C–N at 1515 cm^{-1}, and 1429 cm^{-1}), confirming the presence of the organic linker. Similarly, peaks corresponding to the metal sites Mn–N were located at 864 cm^{-1}, Ni–N at 549 cm^{-1}, and M–O–M/M–O (where M = Co and Ni) at 660 cm^{-1}, verifying the creation of a dual-functional well-coordinated trimetallic MOF structure.[66–68] The conductive framework in supercapacitors enables swift charge transfer, reversible redox (oxidation and reduction) reactions (Co^{2+}/Co^{3+} and Ni^{2+}/Ni^{3+}), and achieves a high specific capacitance (C_s) of 1070 F g^{-1} (CV, 2 mV s^{-1}) and 840 F g^{-1} (GCD, 0.5 A g^{-1}). The unsaturated metal sites and M–O–M bridges collaborate to reduce kinetic barriers in water splitting, thereby effectively catalyzing the oxygen and hydrogen evolution reactions. This results in ultra-low overpotentials (η) of 61 mV for the OER and 47 mV for the HER at a current density (j_{10}) of 10 mA cm^{-2}.

3.1.3 SEM and EDX analysis. A detailed SEM–EDX study of the compositions S_1, S_2, S_3 and S_4 discloses the composition-controlled morphological evolution controlling the electrochemical performance (Fig. 3). S_1 shows disordered nanostrips with low interconnectivity (Fig. 3(a) and (b)), indicating low crystallinity due to the unoptimized Mn content reducing the conductivity and stability. Elemental mapping verifies the homogeneous Ni/Co/Mn/O distribution despite structural flaws (Fig. 3(c1)–(c4)). The best-performing sample, S_2, consists of ultrathin serrated nanostrips with an average diameter of 7.9 nm, as shown in (see Fig. S5), forming a hybrid nanostructure characterized by sawtooth-like edges (Fig. 3(d) and (e)). The ultrathin diameter, together with the increased porosity, ensures facile electrolyte accessibility. Meanwhile, the serrated edges provide abundant catalytic sites, further supported by the homogeneous elemental dispersion (Fig. 3(f1)–(f4)). Inclusion of more Mn to form S_3 produces partially aligned nanostrips (Fig. 3(g), (h) and (i1)–(i4)) with some residual stacking, comparatively modestly enhancing dispersibility when compared to S_4 aggregated nanostrips (Fig. 3(j), (k) and (l1)–(l4)) where too much Mn encourages intralayer coordination at the cost of interlayer spacing. The morphological advantage of S_2 stems from the (i) optimal metal stoichiometry, achieving structural integrity and exposing active sites; (ii) hierarchical porosity, facilitating effective mass/charge transport; and (iii) serrated nanostrips morphology, avoiding

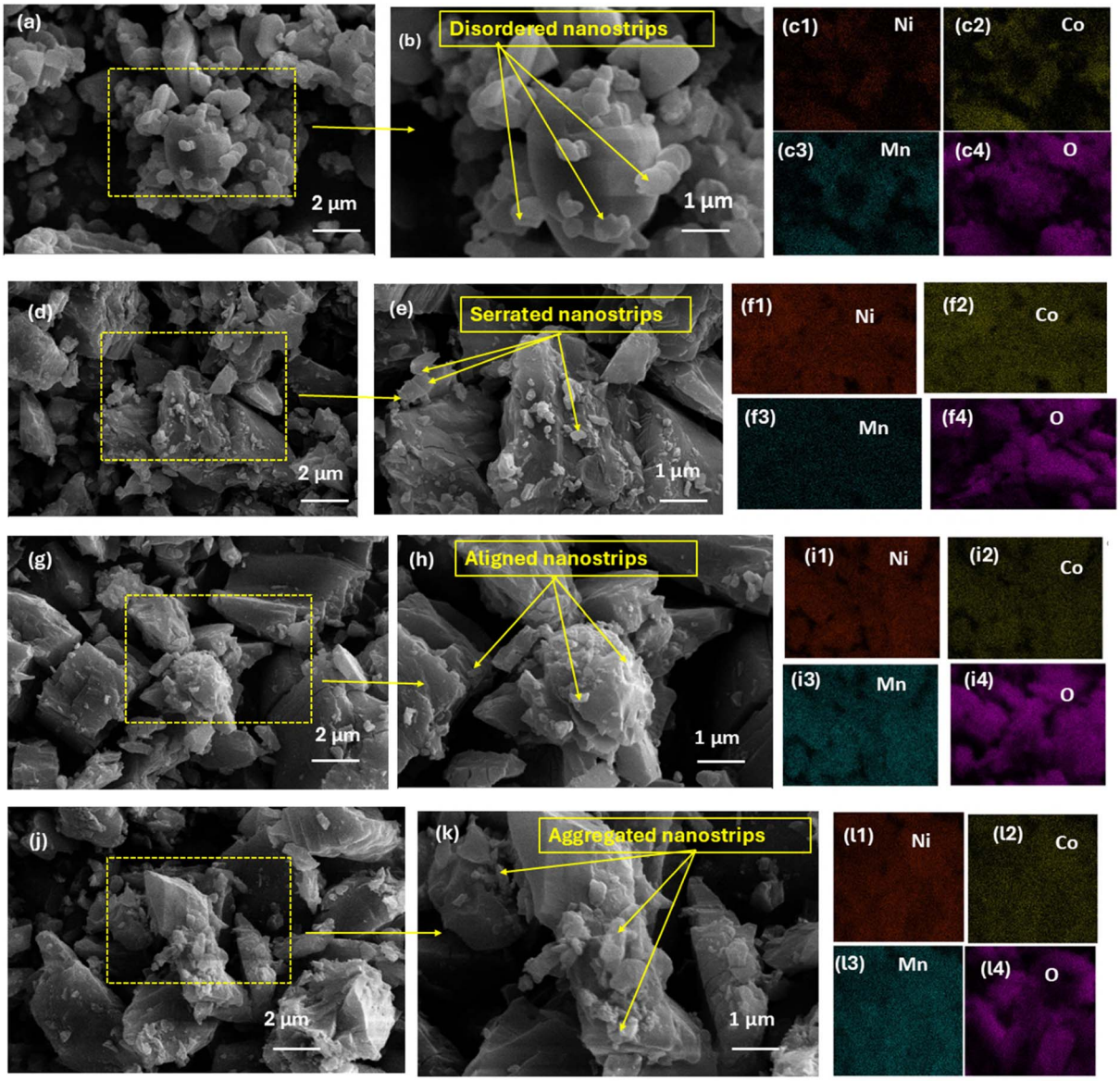

Fig. 3 SEM images and EDX elemental mappings of compositions S_1, S_2, S_3 and S_4. SEM micrographs for S_1 at (a) small and (b) large-magnification, and its elemental area mapping using EDX (c1)–(c4). SEM micrographs and EDX mapping of S_2 (d), (e) and (f1)–(f4). SEM micrographs and EDX mapping (g), (h) and (i1)–(i4) for S_3. SEM micrographs and EDX mapping for S_4 (j), (k) and (l1)–(l4).

fragmentation and too much stacking, essential for supercapacitor and electrocatalytic activity.

3.1.4 BET surface area and porosity analysis. Nitrogen adsorption–desorption isotherms were recorded at 77 K to investigate the surface and textural properties of the catalysts (see Fig. S10(a)). All samples (S_1–S_4) display Type IV isotherms with H3-type hysteresis loops, characteristic of mesoporous materials. The adsorption volume increases gradually with relative pressure (P/P_0), indicating multilayer adsorption and pore-filling behavior. Among the samples, S_2 shows the highest nitrogen uptake, signifying a larger accessible surface area and enhanced porosity compared to the others. Similarly, the porosity index (see Fig. S10(b), calculated as the ratio of the total pore volume ($cm^3\ g^{-1}$) to the BET surface area ($m^2\ g^{-1}$), provides a comparative measure of the overall porosity. The values follow the order $S_2 > S_1 > S_4 > S_3$, with S_2 exhibiting the maximum index (8.75×10^{-4}), further confirming its well-developed pore structure. These metrics highlight the enhanced textural properties of S_2, which facilitate greater active site availability and ion diffusion, correlating directly with its superior performance in water splitting (*e.g.*, lower overpotentials) and supercapacitor applications (*e.g.*, higher specific capacitance).

3.1.5 XPS analysis and valence state investigation of Ni–Co–Mn–PDC MOFs. To gain deeper insight into the oxidation states and electronic environments of the metal centers, detailed X-ray photoelectron spectroscopy (XPS) analyses were conducted for all four Ni–Co–Mn–PDC MOF compositions (S_1–S_4), as presented in Fig. S11–S15. The Ni 2p spectra

(Fig. S11) exhibit well-defined peaks at binding energies around 855.6 eV and 873.4 eV, corresponding to Ni $2p_{3/2}$ and Ni $2p_{1/2}$, respectively, along with distinct satellite peaks, confirming the coexistence of Ni^{2+} and Ni^{3+} species across all samples. Similarly, the Co 2p spectra (Fig. S12) show characteristic doublets for Co $2p_{3/2}$ (~780.2 eV) and Co $2p_{1/2}$ (~795.3 eV), accompanied by shake-up satellite peaks, signifying the presence of both Co^{2+} and Co^{3+} oxidation states. The Mn 2p spectra (Fig. S13) further reveal multiple oxidation states, with Mn $2p_{3/2}$ and Mn $2p_{1/2}$ peaks observed near 641.8 eV and 653.3 eV, respectively, indicating a mixture of Mn^{2+} and Mn^{3+} species. This multivalence is critical for enabling fast redox transitions and efficient charge transfer during electrochemical processes. Notably, a comparative analysis of S_1–S_4 demonstrates that the S_2 composition exhibits a balanced ratio of mixed-valence species for all three metals, suggesting an optimized redox environment that promotes synergistic electron exchange. This observation aligns with the superior electrocatalytic and energy storage performance of S_2 reported in the main text. In addition, the O 1s spectra (Fig. S14) display two major components centered at approximately 531.3 eV and 533.4 eV, corresponding to lattice oxygen (oxygen vacancies) and surface-adsorbed oxygen species (O–C=O), respectively. Among all samples, S_2 exhibits the highest intensity of oxygen vacancy-related peaks, indicating abundant defect sites that enhance the electrical conductivity and facilitate rapid ion diffusion. Collectively, these XPS results confirm the presence of multiple oxidation states (Ni^{2+}/Ni^{3+}, Co^{2+}/Co^{3+}, Mn^{2+}/Mn^{3+}) and oxygen vacancies across all compositions, with S_2 demonstrating the most favorable electronic structure and defect chemistry for efficient redox kinetics, thereby validating its optimized performance in both water splitting and hybrid supercapacitor applications.

3.2 Electrochemical characterization

3.2.1 Electrocatalytic water splitting

3.2.1.1 LSV and Tafel analysis. The performances of the HER and OER for the NiCoMn–PDC MOF/NF electrodes were comprehensively investigated in 1 M KOH using a three-electrode assembly (Fig. 4). To analyze the electrocatalytic properties of the synthesized materials, the overpotential was defined as the potential necessary to achieve current densities (j_{10}) of 10 mA cm^{-2}. The overpotential, determined relative to the RHE applying the Nernst equation, is a crucial criterion that reduces the energy barrier and promotes chemical processes. For the HER (Fig. 5(a)), sample S_2 exhibited better outcomes with a remarkable low recorded overpotential (η) of 47 mV at current densities (j_{10}) of 10 mA cm^{-2}, exceedingly far from those of the S_1 (64 mV), S_3 (57 mV), and S_4 (165 mV) counterparts. Composition S_2 exhibited a significantly lower overpotential than the other compositions, indicating superior performance for hydrogen evolution. Using the following eqn (7), we can gain more insight into the catalyst rapid kinetics and efficiency by calculating its Tafel slopes from polarization curves.[69]

$$\eta = a + b\log(j) \tag{7}$$

In this context, b shows the importance of the Tafel slope, while j represents the current density. Among the studied compositions, S_4 exhibits the lowest Tafel slope (351 mV dec^{-1}) when compared with that for S_3, S_1, and S_2, which show 1009, 913, and 595 mV dec^{-1}, respectively (Fig. 5(c)). Although these absolute values are higher than those typically observed for the state-of-the-art HER catalysts, the relative decrease for S_4 suggests comparatively enhanced ion/charge transfer kinetics within this series, thereby indicating the improved electrocatalytic activity of the NiCoMn-MOF material. The Tafel parameters provide mechanistic insight into whether the HER progresses *via* the discharge ion stage or the combination pathway. In an alkaline medium, the HER can arise in three ways.[68]

Tafel reaction mechanism (30 mV dec^{-1}, combination step):
$H_{(ads)} + H_{(ads)} \rightarrow H_2$

Mechanism of the Volmer reaction
(120 mV dec^{-1}, discharge step): $H_2O + e^- \rightarrow OH^- + H_{(ads)}$

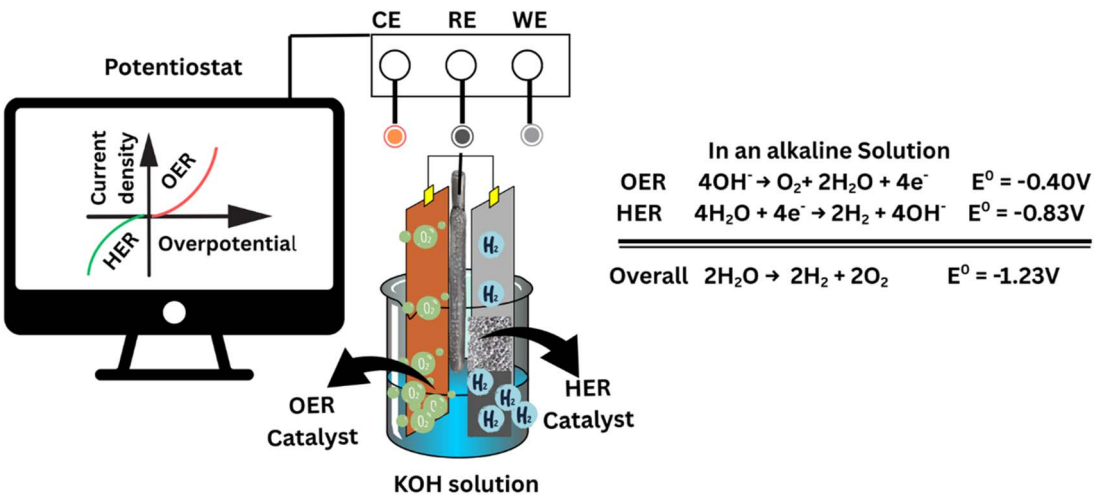

Fig. 4 Three-electrode setup used for electrocatalytic water splitting.

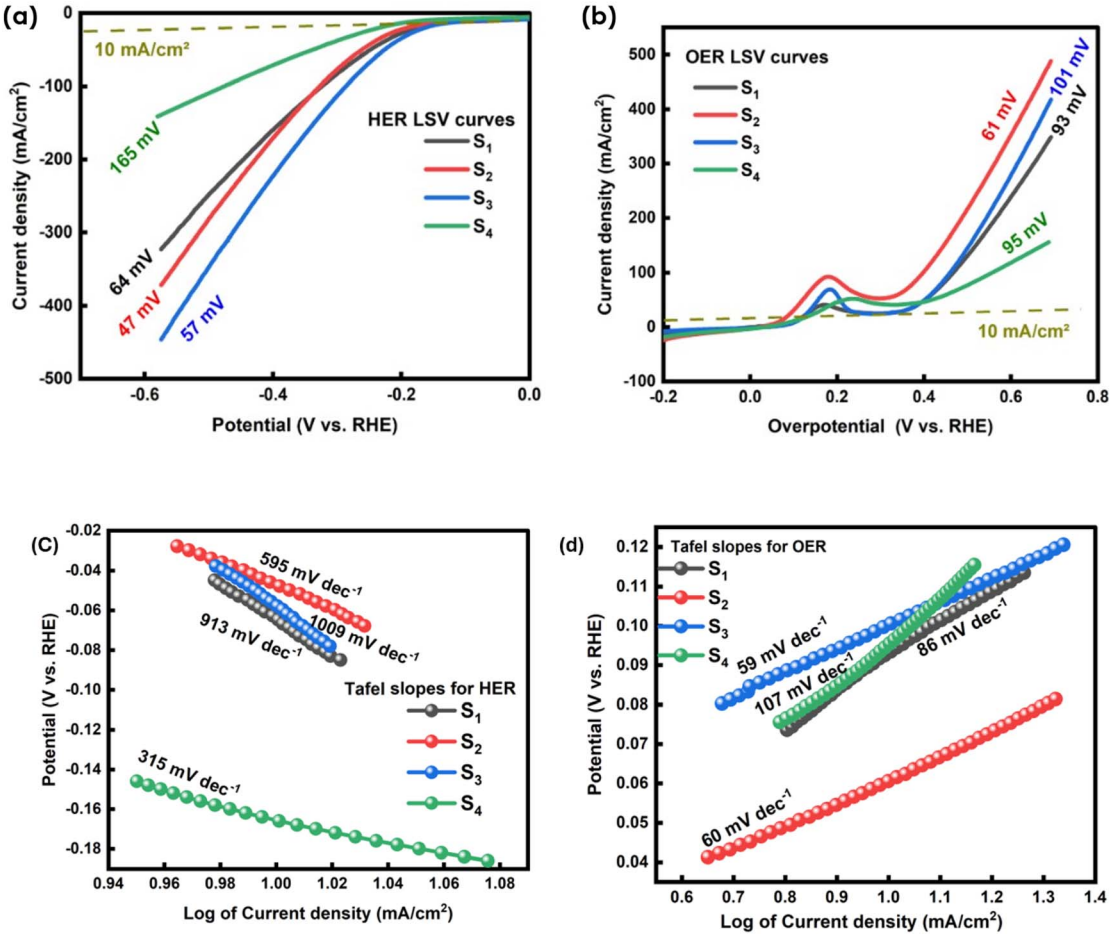

Fig. 5 (a) Polarization curves of the Ni–Co–Mn–PDC MOF for the HER. (b) LSV curves for the oxygen (O_2) evolution response of the as-prepared catalysts. (c) HER Tafel plots. (d) OER Tafel slopes.

Mechanism of the Heyrovsky reaction (40 mV dec^{-1}, ion step):

$$H_{(ads)} + H_2O + e^- \rightarrow H_2 + OH^-$$

When the Tafel slope is less than or equal to 30 mV dec^{-1}, the hydrogen evolution reaction responses may result in the Tafel-step mechanism pathway. Similarly, if the value is 40 mV dec^{-1}, it may indicate the Heyrovsky-step mechanism, while a slope beyond 40 mV dec^{-1} suggests the Volmer-step mechanism, along with the rate-finding steps. The NiCoMn-MOF exhibits extraordinary behavior towards the HER mechanism. The organic linker (pyridine dicarboxylic acid) is primarily responsible for the unusual behavior of NiCoMn-MOFs compared to other materials. As illustrated in Table 2, the diverse connecting groups give MOFs their varied electrocatalytic characteristics. The inclusion of nitrogen in the pyridine ring of the PDC linker accelerates the chemical kinetics, leading to efficient hydrogen evolution. The carboxylic acid

Table 2 OER and HER performance comparison of different MOF-based catalysts

	Tafel slope (HER/OER) (mV dec^{-1})		Overpotential (HER/OER) (mV)				
MOF electrocatalyst	HER	OER	HER	OER	Current density (mA cm^{-2})	Substrate	References
NiCo–HMT MOF/NF	76	86	274	330	30	NF	68
NiCo–PDC MOF/NF	89	73	263	420	30	NF	69
Co-bilinker with PDC	44.4	73.3	151.7	180	10	NF	60
NC@CoO/NF		—	139	290	10	NF	70
$Co(Ni)O_x@CoP_{x-3}$	19.12	108.42	97	309	10	NF	71
Mn-doped NiCo-MOF	89	53	86	220	10	—	72
NiCoMn–PDC MOF/NF	595	60	47	61	10	NF	This work

group serves as both a proton donor and acceptor, playing a crucial role in proton reduction processes. The active involvement of carboxylic acid enhances the overall efficiency of the Ni–Co–Mn–PDC MOF.

In addition to the hydrogen (H_2) evolution reaction, all compositions were evaluated for oxygen (O_2) evolution reactions in an alkaline medium. The OER characterization (Fig. 5(b)) revealed that S_2 operates at current density (j_{10}) and overpotential of only 61 mV with a Tafel slope of 60 mV dec^{-1}, as shown (Fig. 5(d)), competing with noble metal standards. The peak at ~1.2 V *vs.* RHE supports Ni^{2+}/Ni^{3+} redox changes. To put the electrocatalytic activity of our Ni–Co–Mn catalyst into perspective, benchmarking against widely accepted reference catalysts was performed using literature-reported values for Pt/C (HER) and IrO_2/RuO_2 (OER). The comparison is summarized Fig. S2. Pt/C displays an overpotential of ~24 mV for the HER at 10 mA cm^{-2}, highlighting its well-known superior activity. For OER, IrO_2 and RuO_2 exhibit overpotentials of ~398 mV and ~247 mV, respectively. In contrast, our Ni–Co–Mn catalyst requires only 47 mV for the HER and 61 mV for the OER at the same current density. These results clearly demonstrate that the Ni–Co–Mn catalyst not only approaches the performance of Pt/C in HER, but also significantly outperforms IrO_2 and RuO_2 in OER, indicating its strong potential as a cost-effective and highly efficient bifunctional electrocatalyst. In addition, to ensure an accurate assessment free from the contribution of non-faradaic oxidation peaks present in the forward scan, the LSV curves were recorded in reverse scan mode. The resulting LSV curves are presented in Fig. S1, where the overpotential (η) is plotted against the current density. The overpotential required to achieve a current density of 10 mA cm^{-2} was determined from these reverse scans. The values for samples S_1, S_2, S_3, and S_4 were found to be 119 mV, 305 mV, 112 mV, and 130 mV, respectively. Similarly, for the HER and OER study, this improved performance of the trimetallic Ni–Co–Mn–PDC MOF is attributed to the following electrocatalyst properties: (1) abundance of active sites attributed to the presence of ternary metals (Ni, Co and Mn), (2) accelerated electron and kinetics of charge transfer, (3) extensive surface area (m^2) and enhanced porosity, and (4) a synergistic effect arising from the interaction of various metals within the synthesized electrocatalyst. Thus, by optimizing the manganese ratio, the compositional tuning of the material improves the electrocatalytic performance of the as-prepared Ni–Co–Mn–PDC MOF.

3.2.1.2 EIS, CV and Cdl analysis. We employed electrochemical impedance spectroscopy (EIS) over a frequency range from (0.1 Hz to 100 kHz) to evaluate the charge transfer kinetics and storage capabilities of the S_1, S_2, S_3, and S_4 electrodes. EIS serves as a widely used method for examining the interactions that occur among electrode materials and electrolyte ions. It provides data about the characteristics of the electrolyte–electrode interface, double-layer capacitance (Cdl), encompassing ion-transfer kinetics, and interface resistance. A small semicircle was observed in the Nyquist plots within the higher-frequency domain (Fig. 6(a) and (b)), indicating a low charge-transfer resistance, which demonstrates the high conductivity of our materials. The interaction points along the *x*-axis in the EIS spectrum bands in the high-frequency region reveal the sample equivalent series resistance (ESR), providing insights into the resistance between the electrolyte and electrode. The ESR values, which are essential for determining the electron transport efficiency, varied with composition (*i.e.*, ESR value 1.0 Ω for composition S_3, 1.5 Ω for S_1, 2.9 Ω for S_2, and 3.6 Ω for S_4). These results demonstrate that S_3 achieves the lowest ESR due to optimal Ni/Co/Mn stoichiometry, indicating superior charge-transfer kinetics.

Experimentally, the electrochemical active surface area (ECSA) was found from the double-layer capacitance (Cdl). To analyze the double-layer capacitance (Cdl) for the HER, we performed cyclic voltammetry (CV) on NiCoMn-MOF. Subsequently, the measurements spanned scan sweeps of 20–120 mV s^{-1} with 20 mV s^{-1} increments within the capacitive potential window of −0.8 to −1.0 V *vs.* RHE for the HER, as illustrated in Fig. 6(c). Similarly, to measure the double-layer capacitance (Cdl) for the OER mechanism, a positive window of 0.1 V to 0.3 V was chosen, as illustrated in Fig. 6(d).

The Cdl data in Fig. 6(e) for the HER show 7, 2, 1, and 3 mF cm^{-2} for compositions S_4, S_2, S_1, and S_3, respectively, confirming their excellent electrocatalytic performance for hydrogen production. Similarly, the Cdl values in Fig. 6(f) for the OER show 11, 50, 37 and 38 mF cm^{-2} for compositions S_1, S_2, S_3 and S_4, respectively, confirming their remarkable electrocatalytic performance for the oxygen evolution reaction. The ESCA was obtained from the cyclic voltammetry results by calculating the double-layer capacitance rate, Cdl, using the following eqn (8).[73]

$$\mathrm{ESCA} = \mathrm{Cdl}/C_s \quad (8)$$

The electrode surface specific capacitance is labelled as C_s. In alkaline media, its value is equal to 0.04 mF cm^{-2}. As a result, the ESCA values for the compositions S_4, S_2, S_1 and S_3 are 175, 50, 25, and 75 cm^2 for the HER and 950 cm^2, 1200 cm^2, 275 cm^2 and 925 cm^2 for the OER, respectively. The higher the ESCA, the better the electrocatalyst performance in HER/OER, as it promotes charge kinetics, adds more active sites, optimizes material deposition, and provides synergistic benefits. In electrochemical processes, reactions occur on the surface of the electrode. The availability of the active sites increases for the reactant molecules to engage with upon increasing the ECSA, thereby accelerating the total reaction rate. The presence of carbon contributes to an additional active site, contributing to an improved ESCA. However, not every carbon active site for the oxygen and hydrogen evolution reactions is catalytically active. The limited catalytic activity of carbon sites supports the hypothesis that metal centers are the primary active sites for the HER and OER.

3.2.1.3 IR compensation, reproducibility with error bar and NF control analysis. The fully corrected kinetic overpotentials of 47 mV for the HER and 61 mV for the OER on composition S_2 were obtained using the iR-compensation method, as defined by eqn (9)–(11).

$$E(\mathrm{measured}) = \eta(\mathrm{kin}) + iR\ (\Omega) \quad (9)$$

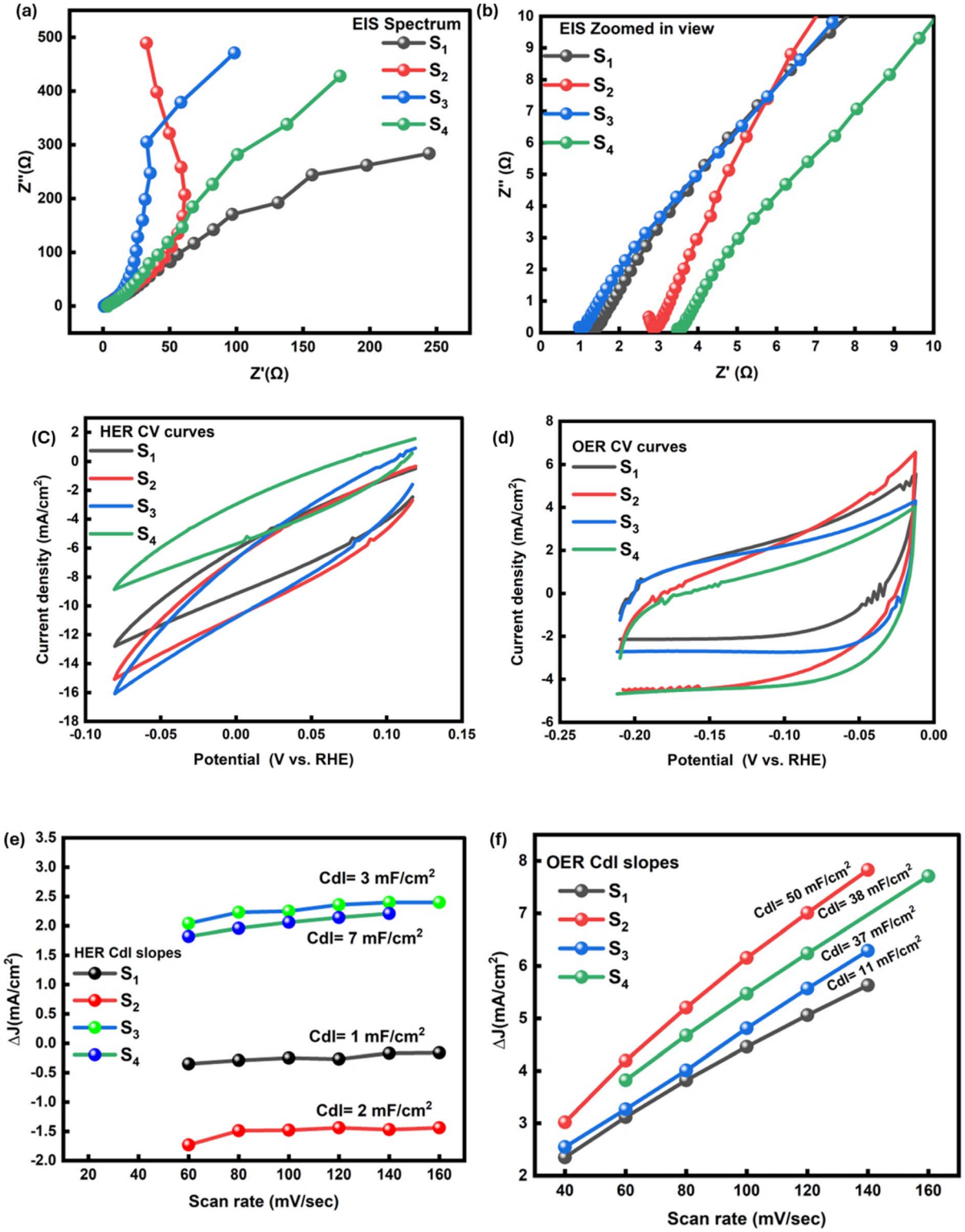

Fig. 6 (a) Nyquist plots (EIS) for S_1, S_2, S_3 and S_4. (b) EIS detailed view (magnified). (c) CV comparison for S_1, S_2, S_3 and S_4 for the HER. (d) CV comparison for S_1, S_2, S_3 and S_4 for the OER. (e) Comparison of the Cdl value of the MOFs for the hydrogen evolution reaction. (f) Comparison of the oxygen evolution Cdl for the MOFs.

$$E(\text{corrected}) = E(\text{measured}) - \beta \times iR\ (\Omega) \quad (10)$$

$$E(\text{corrected, full}) = E(\text{measured}) - iR\ (\Omega) \quad (11)$$

The uncompensated solution resistance was measured by EIS (~2.9 Ω), giving an ohmic drop of ~29 mV at 10 mA cm^{-2}. For the optimized S_2 sample, the raw measured overpotentials were 76 mV for the HER and 90 mV for the OER. After 90% iR

correction, the values decreased to 49.9 mV (HER) and 63.9 mV (OER), and the fully corrected kinetic overpotentials were 47 mV (HER) and 61 mV (OER), as illustrated in Fig. S6. These results confirm that the excellent catalytic activity of S_2 originates from its intrinsic properties, rather than measurement artifacts.

To ensure reproducibility and statistical reliability of the electrochemical performance, four independent NiCoMn–PDC MOF electrodes were fabricated and tested under identical conditions for both the hydrogen evolution reaction (HER) and oxygen evolution reaction (OER). The measured overpotential values (at the target current density) were 203, 209, 196, and 158 mV for HER, and 250, 99, 67, and 306 mV for OER. The corresponding mean overpotentials were 191.5 ± 22.95 mV (HER) and 180.5 ± 115.62 mV (OER). These results, represented as bar graphs with error bars in Fig. S7, demonstrate the consistency of the catalytic performance across multiple electrodes. Overall, these findings confirm the statistical reproducibility and robust electrocatalytic performance of the NiCoMn–PDC MOF system.

To evaluate the intrinsic catalytic activity and establish a reliable control, additional hydrogen and oxygen evolution reaction (HER and OER) measurements were performed using bare Ni foam (NF) under identical experimental conditions. The corresponding linear sweep voltammetry (LSV) curves for all four samples (S_1–S_4) and NF are shown in Fig. S8(a) and (b), respectively. For the HER, the overpotentials required to achieve a current density of 10 mA cm^{-2} are 64 mV (S_1), 47 mV (S_2), 57 mV (S_3), 165 mV (S_4), and 179 mV (NF). Meanwhile, for the OER, the values are 93 mV (S_1), 61 mV (S_2), 101 mV (S_3), 95 mV (S_4), and 99 mV (NF). The LSV curves clearly indicate that all modified samples exhibit lower overpotentials and higher current responses than bare NF, demonstrating their improved electrocatalytic activity. Among them, S_2 shows the lowest overpotentials for both the HER and OER, confirming its superior bifunctional catalytic performance relative to the NF control.

3.2.1.4 Stability and durability analysis. To further evaluate the long-term stability and durability of the NiCoMn–PDC MOF as a bifunctional electrocatalyst, chronoamperometry tests were conducted for 14 hours in 1 M KOH electrolyte. For the HER, the test was performed at a constant potential of −0.47 V *vs.* RHE, corresponding to an initial current density of approximately −10 mA cm^{-2}. As shown in Fig. S9(a), the current density exhibited a slight initial fluctuation before stabilizing, retaining nearly 100% of its initial value after 14 hours of continuous operation, as indicated by the arrow. This minimal decay underscores the robust structural integrity of the trimetallic MOF framework, likely attributed to the synergistic Ni–Co–Mn coordination and the rigid PDC linker, which prevent significant dissolution or morphological changes under reductive conditions.

Similarly, for the OER, chronoamperometry was carried out at 0.61 V *vs.* RHE, achieving an initial current density of around 10 mA cm^{-2}. The profile in Fig. S9(c) reveals excellent retention, with the current density maintaining approximately 100% of its starting value over the 14 hours period, demonstrating superior tolerance to oxidative environments. The negligible degradation highlights the catalyst's ability to sustain active sites for multi-electron transfer processes, outperforming many reported monometallic and bimetallic MOFs that suffer from faster deactivation due to phase transformations or metal leaching.

To corroborate these findings, LSV polarization curves were recorded before and after the 14 hours stability tests. For the HER (Fig. S9(b)), the curves before and after chronoamperometry nearly overlap, with only a marginal shift in the overpotential (less than 10 mV at 10 mA cm^{-2}), confirming that the electrocatalytic activity remains largely intact. In the case of the OER (Fig. S9(d)), the pre- and post-stability LSV curves show even closer alignment, with no significant increase in the overpotential, further validating the catalyst's durability. This exceptional long-term performance can be ascribed to the high electrochemical active surface area (ECSA) and the favorable electron transfer kinetics facilitated by the 3D nanostructure of the NiCoMn–PDC MOF, as previously evidenced by the low Tafel slopes (595 mV dec^{-1} for the HER and 60 mV dec^{-1} for the OER) and substantial double-layer capacitances (2 mF cm^{-2} for the HER and 50 mF cm^{-2} for the OER). Such stability is crucial for practical applications in alkaline water electrolysis, where prolonged operation under high current densities is essential for efficient hydrogen production. Overall, these results position NiCoMn–PDC MOF as a promising, cost-effective alternative to noble metal-based catalysts for sustainable energy conversion.

3.2.2 Energy storage analysis

3.2.2.1 Cyclic voltammetry (CV) analysis. We performed cyclic voltammetry in a one molar (1 M) KOH solution over a potential of 0–0.7 V, with a scan sweep varying from 2 to 50 mV s^{-1} in a three-electrode (3E) assembly. The CV profiles of the compositions exhibit distinct redox peaks, as seen in Fig. 7(a)–(d). The redox peaks, as shown by faradaic processes in M–O–ON/M–O (where M = Mn, Co, or Ni; N = H or K), indicate pseudocapacitive behavior. The specific capacitance decreases, but the current increases when the scan rate increases from 2 to 5 mV s^{-1}, a trend that was observed for all the compositions. This behavior is linked to the inadequate time for the electrolyte ions to interact effectively with the electrode material. The CV responses of the composition (S_1) with unoptimized manganese content, as shown in Fig. 7(a), exhibit the smallest area (m^2) under the curve as verified from the lowest specific capacitance (C_s) of 350 F g^{-1}. Similarly, the composition (S_3), with a moderate Mn amount, shows a better area under the CV curve but a limited specific capacitance (C_s) value of 366 F g^{-1}, indicating inefficient ion kinetics as seen in Fig. 5(b). In contrast, the composition (S_4) with the highest manganese content, as shown in Fig. 7(c), displays a greater specific capacitance (C_s) of 727 F g^{-1} in comparison to S_1 and S_3, as indicated by the increase in the CV area. Remarkably, the best composition (S_2), as shown in Fig. 5(b), displays the highest specific capacitance (C_s) of 1070 F g^{-1} because of its expanded CV area and intensified redox peaks facilitated by the optimization of the Mn content.

The comparative analysis of the CV profiles in Fig. 7(e) for all samples provides a direct illustration of the charge storage performance, clearly differentiating the electrodes, where S_2 exhibits the largest integrated area, followed by S_4, S_3, and

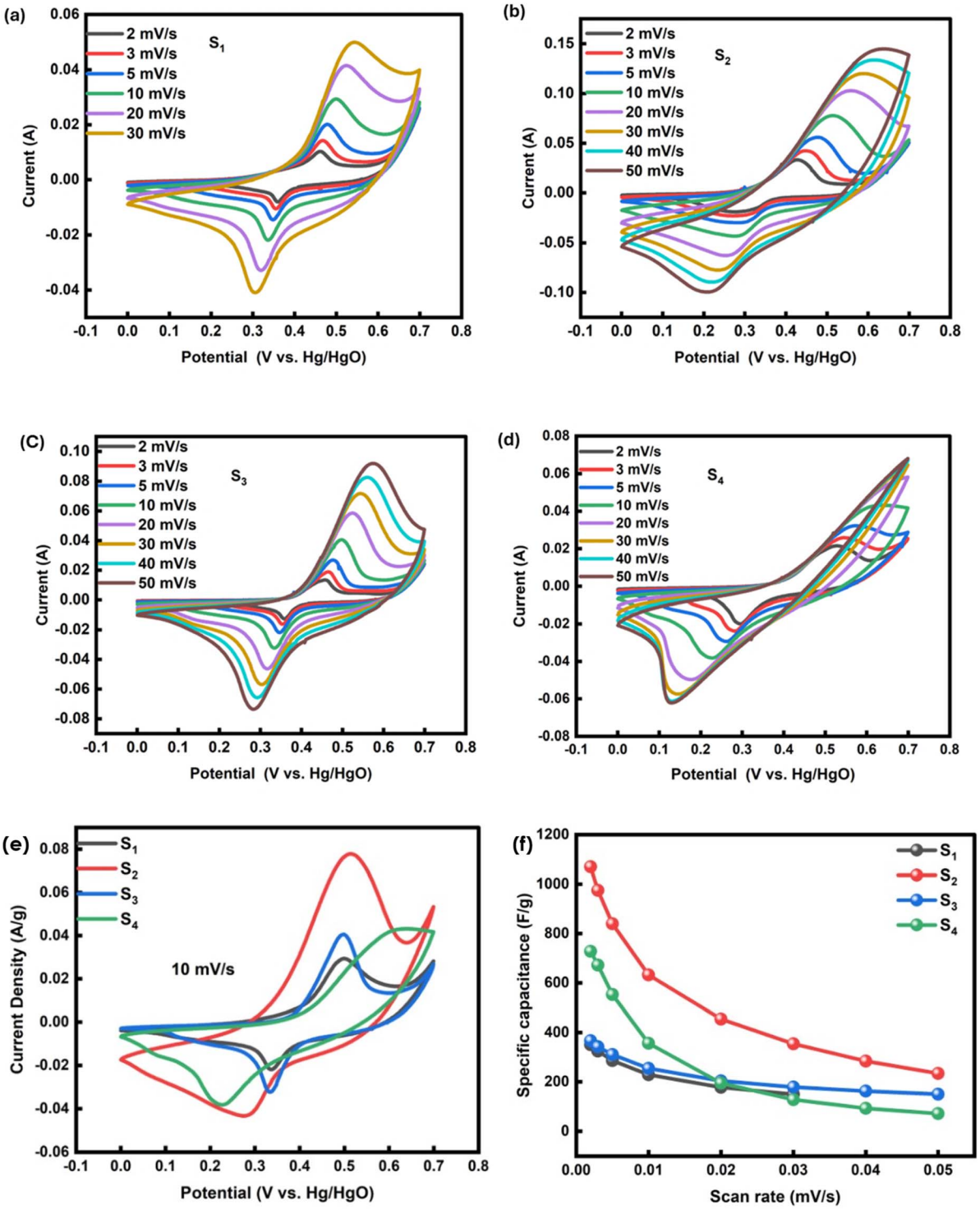

Fig. 7 CV of all compositions: (a) S_1 with the lowest Mn content, (b) S_2 with the best composition, (c) S_3 containing a moderate amount of Mn, and (d) S_4 containing the maximum Mn content. (e) Comparison of CV curves for all samples at fixed scan rate. (f) Comparison of the specific capacitance from CV.

finally S_1 with the smallest area. The largest CV area, as clarified by specific capacitance values plotted in Fig. 7(f), reveals the S_2 superior specific capacitance (C_s) of 1070 F g^{-1} compared to those of S_4, S_3, and S_1. The expanded CV area intensified the redox peaks, and the outstanding specific capacitance of S_2 verified the optimized manganese content within the Ni–Co–Mn-MOF structure. This metal optimization not only maximizes the synergistic interplay between metals, but also leads to active site exposure, which increases the redox activity and charge transfer kinetics.

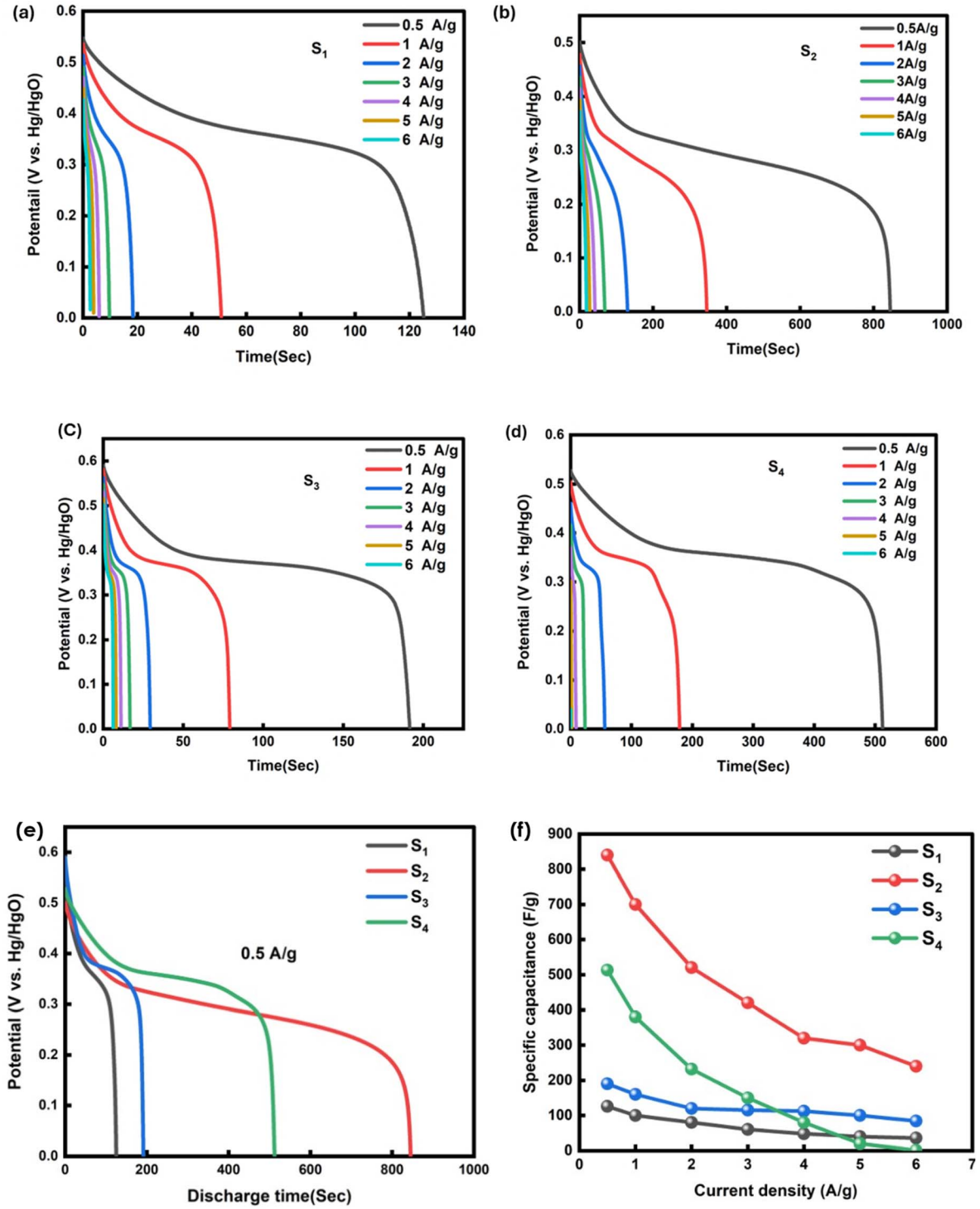

Fig. 8 Discharging cycle of all compositions: (a) $S_1(Mn_{0.25})$, (b) S_2(optimized), (c) $S_3(Mn_{0.75})$, and (d) $S_4(Mn_1)$. (e) Comparison of the discharge cycle for all compositions. (f) Comparison of the specific capacitance from GCD for all compositions.

3.2.2.2 Galvanostatic charge–discharge (GCD) analysis. GCD measurements were performed on each of the four electrodes to examine the charge–discharge behavior. The discharge profile of the electrode material was recorded within the potential window from 0 to 0.5 V, exhibiting a progressive decrease in discharge duration as the current density (j_{10}) varied from 0.5 to 6 A g^{-1}, as shown in Fig. 8(a) to (d). The common trend of decreasing discharge time as current density increases arises from insufficient ion diffusion kinetics at higher densities, a characteristic limitation commonly observed in energy storage devices. This behavior is characteristic of energy storage systems, where ionic mobility is restricted upon an increase in

the current density, resulting in a shorter discharge duration. Consequently, during redox processes, charge storage becomes confined to the electrode surface layer. The specific capacity (C g^{-1}) is the most direct performance indicator derived from the GCD discharge curve at a given current density. A higher specific capacity of the electrode material indicates a higher charge storage capability. The specific capacity (Q_s) values of the electrode materials S_1, S_2, S_3, and S_4 confirm the strong dependence on the manganese (Mn) content within Ni–Co–Mn-MOF. Composition S_1, as shown in Fig. 8(a), contains the unoptimized Mn content, which exhibits the lowest specific capacity of 62 C g^{-1}. This not only indicate a minimal charge storage capability, but also suggest insufficient redox-active material or poor conductivity. Similarly, as seen in Fig. 8(c), composition (S_3) with moderate Mn content displays a modestly improved specific capacity of 95 C g^{-1} compared with S_1, suggesting the beneficial redox contribution from Mn. Likewise, composition (S_4) with the highest Mn content, as illustrated in Fig. 8(d), delivers a higher specific capacity of 255 C g^{-1} than S_1 and S_3, demonstrating the critical role of Mn in providing significant redox activity in terms of pseudocapacitance for charge storage. Notably, as shown in Fig. 8(b), the optimal composition (S_2) achieves the peak outcome with a specific capacity (Q_s) of 420 C g^{-1}, which even exceeds that of S_4. This highlights that there is an optimal Mn content within Ni–Co–Mn-MOF that maximizes charge storage.

The GCD discharge curves comparison, as shown in Fig. 8(e) for compositions S_1–S_4, provides a direct analysis of their charge storage capabilities at a given current density. The specific capacitance values, as illustrated in Fig. 8(f), quantify the outcome of the electrode because a higher specific capacitance indicates greater energy storage capabilities. A higher specific capacitance of 840 F g^{-1} was observed for composition (S_2) compared with S_1 (126 F g^{-1}), S_3(190 F g^{-1}), and S_4 (513 F g^{-1}) and also with recent literature (Table 3). This confirmed its status as the best electrode material as a result of its optimized Mn loading, which not only maximizes the density of accessible and electrochemically active redox sites but also electronic conductivity throughout the electrode structure.

Table 4 Comparative analysis of EIS for compositions S_1, S_2, S_3, and S_4 across various parameters and for the hybrid supercapacitor device before and after five thousand cycles

Material	Name	R_s (Ω)	R_{ct} (Ω)	Z_W (Ω)
$NiCoMn_{0.25}$–PDC	S_1	3.641	12.47	262.2
$NiCoMn_{0.5}$–PDC	S_2	2.668	27.49	0.00000029
$NiCoMn_{0.75}$–PDC	S_3	3.538	10.66	0.0000068
$NiCoMn_1$–PDC	S_4	2.916	9.99	0.000000074
Before stability	Before	1.375	12.71	0.00000012
After stability	After	1.633	13.34	0.000000013

3.2.2.3 Electrochemical impedance spectroscopy (EIS) characterization. The Nyquist plot is used for analyzing the electrochemical impedance (EIS) characteristics of working electrode materials (S_1–S_4) across a range of frequencies. The examination of the plot facilitates an understanding of the Warburg resistance (Z_W), charge transfer resistance (R_{ct}), and solution resistance (R_s) associated with supercapacitor electrodes. ESR means equivalent series resistance, which reveals the total resistance within a system, encompassing the resistance of the electrolyte, the contact resistance between the current collector and the electrodes, and the resistance of the materials involved. Analysis of Nyquist plots enhances our understanding of the operational behavior of electrode materials and impedance characteristics. Fig. 6(a) shows the Nyquist plots for compositions S_1, S_2, S_3, and S_4 over the tested frequencies from 0.1 Hz to 100 kHz. The plot in Fig. 6(b) enabled us to obtain exact values of ESR: 1.0 Ω for S_3, 1.5 Ω for S_1, 2.9 Ω for S_2, and 3.6 Ω for S_4. Similarly, through software, R_s, R_{ct}, and Z_W values were calculated for every electrode, as summarized in Table 4. The values of R_s 3.641 Ω, 2.668 Ω, 3.538 Ω, and 2.916 Ω were determined for electrodes S_1, S_2, S_3, and S_4, respectively. Accordingly, the best composition (S_2) with the smallest R_s (2.668 Ω) indicates better electrolyte accessibility and contact at the electrode–electrolyte interface to achieve high rates. Consequently, the material reaches the highest capacitance (840 F g^{-1}) due to reduced resistance. Electrodes made by

Table 3 Comparison of the charge storage performance obtained in this work with those of the previously reported works

Materials	Electrolyte	3E-Specific capacitance (F g^{-1}) at current density (A g^{-1})	Energy density (Wh kg^{-1})	Power density (W kg^{-1})	Cyclic stability (%)	References
NiCoCu LDH	1 M KOH	807 at 0.5	22.4	1275	95% after 4000	63
MWCNT/MOF-67	1 M KOH	464 at 0.5	13.14	616	89% after 7000	74
NiCoMn-MOF	3 M KOH	1905 at 1	61.52	6945.4	97% after 15 000	75
$Ni_2Co_{0.75}Mn_{0.25}$-MOFs	3 M KOH	1428 at 1	38.10	884.38	83.5% after 3000	76
$Cu(Co–Ni)_2S_4$ NTs/Ni	1 M KOH	382.1 at 2	0.27	21.75	95.8% after 5000	77
NiCoMn–OH	1 M KOH	2098.2 at 1	50	850	73.6% after 6000	78
Ni–Co–Cu–OH	6 M KOH	1122.97 at 1	52.66	7500	92.2% after 10 000	79
NiCo-MOF	6 M KOH	1234 at 1.0	—	—	91% after 5000	64
NiO/CuO-MOF	6 M KOH	735 at 0.5	—	—	—	80
Co–Ni-MOF@rGO	1 M KOH	1260.8 at 1	319.21	64.29	98.3% after 7000	81
CoNi-MOF	1 M H_2SO_4	2154.0 at 1	138.0	800.0	76.7% after 10 000	82
Ni–Co MOF	6 M KOH	318 at 1	—	—	60% after 10 000	83
NiCo-MOF	1 M KOH	1333 at 2	28	444	83% after 2000	84
Cu/Co-MOF	2 M KOH	3150 at 1	73.19	849.94	96.74% after 10 000	85
NiCoMn–PDC MOF/NF	1 M KOH	840 at 0.5	45	475	79% after 5000	This work

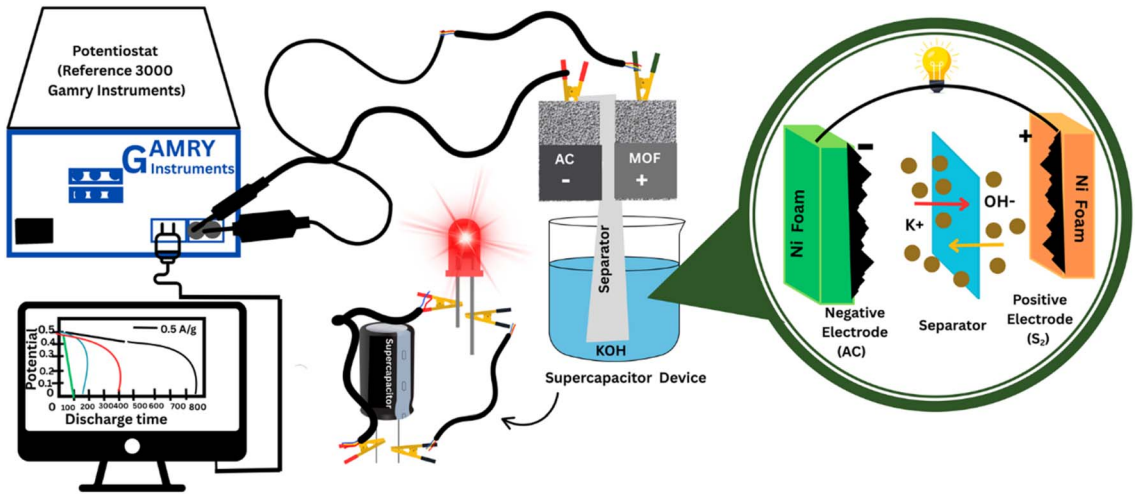

Fig. 9 Hybrid supercapacitor device tested with help of the two-electrode configuration.

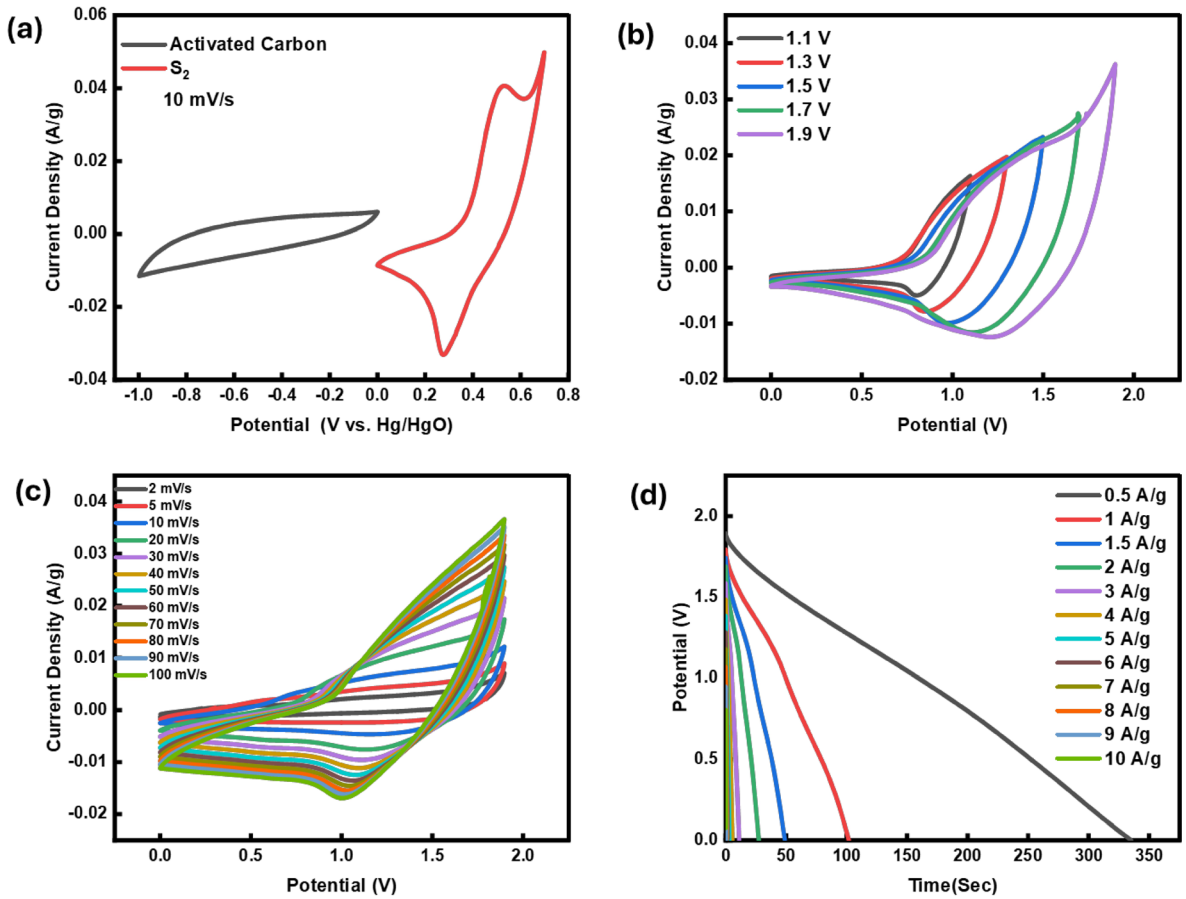

Fig. 10 (a) In electrode assemblies (2E), CV of AC and S_2 at 10 mV s^{-1}. (b) Hybrid supercapacitor device's CV carried out at a scan sweep of 30 mV s^{-1}. (c) CV profiles of the device at 1.7 V with scan rates changing from 5 to 100 mV s^{-1}. (d) Within a specific potential window of (1.65 V), the discharge profiles of the hybrid supercapacitor device at different current densities.

NiCoMn–PDC MOFs exhibit low resistance (R_s), enabling their effective use in supercapacitors applications.

3.2.3 Two-electrode supercapacitor device (MOF//AC) analysis

3.2.3.1 Device CV, GCD, specific capacitance and Ragone plot analysis. We conducted a research study to investigate the potential applications of the optimized MOF composition (S_2). We assembled a hybrid supercapacitor using a manufactured cell with a negative electrode made from activated carbon (AC), while the positive electrode from the best material composition (S_2). A filter paper was placed between the two electrodes to facilitate the passage of ions. The high porosity promotes ionic transport, while its mechanical strength and chemical inertness assure stability and compatibility with the system (refer to Fig. 9). Voltage allocation was calculated using the two electrode capacitance values. To maximize the performance of the active material in a hybrid supercapacitor device, it is crucial to establish a uniform allocation of potential and optimize the mass of material utilized in both electrodes. In this work, both electrodes were assembled with equal mass loadings (12 mg cm^{-2}) using the mass balance relation ($m^+C^+\Delta V^+ = m^-C^-\Delta V^-$), which provided reasonable charge balance and stable performance to further enhance the energy efficiency.[86] Fig. 10(a) illustrates the CV curves obtained for AC at the potential window of −1 to 0 and CV curves for S_2 at the potential window of 0 to 0.7 in a two-electrode (2E) system when scanning at 10 mV s^{-1}. A quasi-rectangular voltammogram for AC confirmed that it behaves as an EDLC. On the other hand, the voltammogram for S_2 revealed redox peaks, indicating that this material participates in both cathodic and anodic reactions, a characteristic of pseudocapacitive behavior. This two-electrode assembly exhibits hybrid behavior. CV was performed on the hybrid device over various voltage ranges at a scan sweep of 30 mV s^{-1}, as illustrated in Fig. 10(b). We repeated the CV at a fixed potential window of 0–1.9 V to investigate the device behavior, as depicted in Fig. 10(c), at scan seeps from 2–100 mV s^{-1}. We reduced the scan speed and then a quasi-rectangular curve was obtained, indicating that the AC electrode EDLC was the primary charge-storage process. As the scan rate increased, the curve exhibited pseudocapacitive behavior of the S_2 electrode, restricting EDLC to low potential levels. At 40 mV s^{-1}, the curve was rectangular up to (0.9 V). However, at (100 mV s^{-1}), it was confined to 0.8 V, accurately predicting the device hybrid charge storage behavior. We evaluated the hybrid supercapacitor energy and power storage capability using the GCD test. The potential window was 0–1.9 V, with the current density ranging from 0.5–10 A g^{-1}. Fig. 10(d) illustrates a consistent decline in voltage over time,

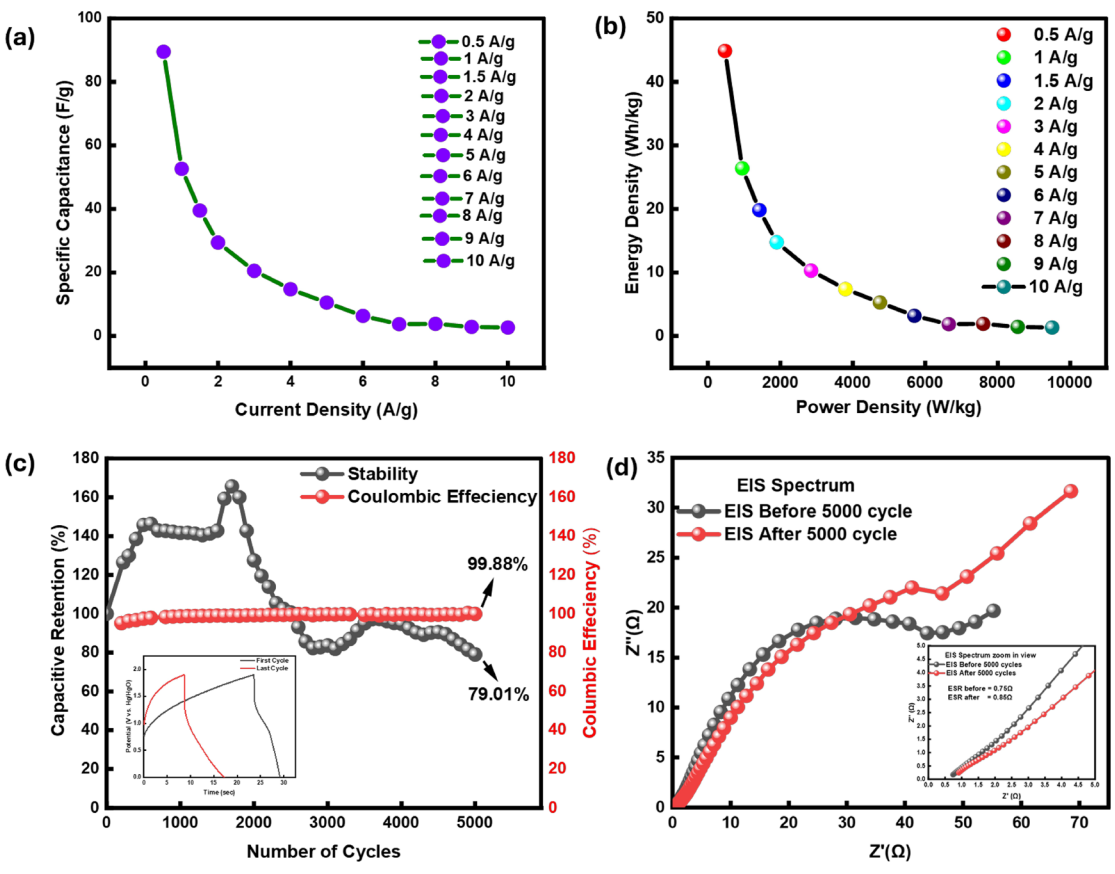

Fig. 11 (a) Specific capacitance with varying current densities, (b) Ragone plot, (c) coulombic efficiency and cyclic stability at 4 A g^{-1} of the hybrid supercapacitor device (AC//S_2), (d) EIS spectra demonstrating the device conductivity *via* plot.

with a little shift in the slope before reaching zero. That resembles hybrid behavior, which is consistent with the CV curves. Eqn (3) calculates the device-specific capacity (see Fig. 11(a)) based on discharge cycles. The device exhibited a specific capacity of 89.4 C g^{-1} at a current density of 0.5 A g^{-1}. The power density and energy density of the hybrid supercapacitor are determined using eqn (5) and (6), respectively, with the results illustrated in the Ragone plot (Fig. 11(b)). The hybrid supercapacitor demonstrates an impressive power density of 475 W kg^{-1} and energy density of 44.86 Wh kg^{-1} at a current density of 0.5 A g^{-1}. For clarity, these values are benchmarked against representative MOF-based and hybrid supercapacitors in the literature, as summarized in Table 3. The hybrid supercapacitor device shows a significantly high-power density of 9500 W kg^{-1} at a high current density of 10 A g^{-1}.

3.2.3.2 Stability, efficiency, impedance analysis and structural characterization of device. The hybrid supercapacitor device stability was evaluated at a current density of 4 A g^{-1} over 5000 GCD cycles. The capacitance of the hybrid device increased to ~170% by cycle 1700, which we attribute to progressive electrode activation and improved electrolyte penetration/wettability, leading to the exposure of additional active sites. After this activation phase, a moderate degradation trend was observed, with retention decreasing to 83% at cycle 3000, recovering to 94% at cycle 4000, and finally stabilizing at 79% by cycle 5000, as shown in Fig. 11(c). This decline is consistent with partial structural rearrangement and a slight increase in the charge-transfer resistance, as evidenced by the Nyquist plots (Fig. 11(d)). The charge transfer resistance increased from 12.71 Ω to 13.34 Ω (Table 4) and ESR from 0.75 Ω to 0.85 Ω, suggesting extended ion/electron transport pathways and minor pore blockage. Despite these changes, the device retained stable performance with an ultrahigh coulombic efficiency of 99.8%, confirming robust electrochemical reversibility.

To evaluate the structural stability, XRD analysis was conducted on the electrode material in both the pre-cycling and post-cycling states. As shown in Fig. S3, the diffraction peaks before and after 5000 charge–discharge cycles are well preserved without any shifts, broadening, or appearance of new peaks. This indicates that the crystalline framework of the electrode remains stable during long-term cycling. The retention of the structural integrity, combined with the observed electrochemical performance, confirms the stability of the electrode material under repeated cycling conditions.

Similarly, SEM and EDX confirm stability after 5000 cycles, as shown in Fig. S4. Pristine SEM (Fig. S4(a and b)) shows the uniform MOF deposition on NF; the post-cycling images (Fig. S4(d and e)) show that the structure is retained without cracking. EDX pre-cycling Fig. S4(c): C 13%, O 12%, F 10%, Co 6%, others likewise; post-cycling Fig. S4(f): O 19%, C 7%, F 8%, others similar. Minor shifts suggest limited surface changes, aligning with a coulombic efficiency of 99.8% and retention of 79% by 5000 cycles, highlighting the MOF robustness for supercapacitors.

4. Conclusions

In this research, we highlighted Ni–Co–Mn–PDC MOF as a novel material that offers a promising response to the challenges arising from the reaction kinetics of electrocatalytic water splitting and energy density of the supercapacitor. Our study focused on the synthesis of transition metal-based ternary MOFs through the hydrothermal method, utilizing 2,6-pyridine dicarboxylic acid as the organic linker. This unique combination overcomes sluggish water-splitting kinetics while enhancing supercapacitor energy density, distinguishing our work from previous studies. The electrochemical analysis indicates a significant enhancement in electrocatalytic performance and charge storage capabilities. Notably, significant achievements include a supercapacitor specific capacitance of 1070 F g^{-1} at 2 mV s^{-1} from CV, 840 F g^{-1} at 0.5 A g^{-1} from GCD, and a specific capacity of 420 C g^{-1}. Analogously, electrocatalytic water splitting results in overpotentials of 61 mV for the OER and 47 mV for the HER at 10 mA cm^{-2}, with a Tafel slope of 60 mV s^{-1}. Furthermore, the hybrid supercapacitor device exhibits a power density of 9500 W kg^{-1} at 10 A g^{-1}, an energy density of 44.86 Wh kg^{-1} at 0.5 A g^{-1} with a coulombic efficiency of 99.88%, and cyclic stability of 79% after 5000 charge–discharge cycles. This finding establishes Ni–Co–Mn–PDC MOF as a highly viable energy material that combines high energy storage with efficient electrocatalysis, due to its low cost, environmentally friendly nature, and favorable electrochemical performance.

Conflicts of interest

There are no conflicts to declare.

Data availability

No external data were used in this study. All the relevant experimental data have already been included and thoroughly discussed in the main manuscript.

Supplementary information: additional electrochemical results and supporting structural and surface characterization data (SEM, XRD, XPS, and BET). See DOI: **https://doi.org/10.1039/d5ra05650k**.

References

1 M. A. Marwat, et al., Novel NiCoMn MOFs/Ag citrate nanocomposites for high-performance asymmetric supercapacitor applications, *Electrochim. Acta*, 2025, **511**, 145373.
2 J. Zhang, H. Ni, J. Yu and B. Zhao, Ni-Doped Co-Based Metal–Organic Framework with Its Derived Material as an Efficient Electrocatalyst for Overall Water Splitting, *Catalysts*, 2025, **15**, 355.
3 D. H. Taffa, D. Balkenhohl, M. Amiri and M. Wark, Minireview: Ni–Fe and Ni–Co Metal–Organic Frameworks for Electrocatalytic Water-Splitting Reactions, *Small Struct.*, 2023, **4**, 2200263.
4 M. Afshan, et al., Electronic modulation of MOF-engineered bimetallic phosphides for cost-effective ampere-level water splitting and continuous hydrogen production via

supercapacitor integration, *J. Energy Chem.*, 2025, **108**, 221–238.
5 S. M. Hashmi, S. Noor and W. Parveen, Advances in water splitting and lithium-ion batteries: pioneering sustainable energy storage and conversion technologies, *Frontiers in Energy Research*, 2024, **12**, 1465349.
6 S. Rohith, et al., Ultrasound-Induced Growth of Co/Ru Bimetallic Metal Organic Framework towards Supercapacitors and Water-Splitting Applications, *J. Inorg. Organomet. Polym. Mater.*, 2025, 1–15.
7 G. B. Bhanuse, S. Kumar, C. W. Chien and Y. P. Fu, Development of heterostructured $ZnCo_2O_4$@Ni-MOF electrode for the asymmetric supercapacitor and electrocatalytic oxygen evolution reaction applications, *Electrochim. Acta*, 2025, **511**, 145371.
8 N. Kumar, P. Bhattacharya, A. Jana and S. Kumar, Synergism induced multifunctional electroactivity of Co-Ni bimetallic metal-organic frameworks towards oxygen evolution reaction and supercapacitors, *Inorg. Chem. Commun.*, 2025, **177**, 114445.
9 Janak, R. Jaryal, Sakshi, R. Kumar and S. Khullar, Nickel(II) and cobalt(II) based 2D mixed metal-metal organic frameworks (MM-MOFs) for electrocatalytic water splitting reactions, *Catal. Today*, 2025, **446**, 115117.
10 M. Mehrpooya, et al., High-performance NiMo@Co@NSC electrocatalyst for efficient overall water splitting, *Int. J. Hydrogen Energy*, 2025, **127**, 1–17.
11 R. Bhabal, S. Gupta, R. Fernandes, M. Gupta and N. Patel, Bifunctional CoPBO/Co-MOF composite electrocatalyst for energy-efficient hydrogen evolution by urea-assisted water splitting, *Int. J. Hydrogen Energy*, 2025, **116**, 299–311.
12 F. Z. Kashani and M. Mohsennia, Enhancing electrochemical hydrogen storage in nickel-based metal-organic frameworks (MOFs) through zinc and cobalt doping as bimetallic MOFs, *Int. J. Hydrogen Energy*, 2025, **101**, 348–357.
13 S. K. Konavarapu, G. Kim, K. Shin and S. Y. Kim, Boosting Electrocatalytic Activity of Bimetallic CoNi-MOF for OER and HER through a Synergistic Bimetallic Approach, *Chem.–Eur. J.*, 2025, **31**, e202500010.
14 B. Dai, et al., Introducing different long-chain flexible ligands to regulate the transformation behavior of NiFe-MOF and as bifunctional catalysts for the HER/OER, *J. Colloid Interface Sci.*, 2025, **682**, 80–93.
15 A. Hu, et al., NiCoFe-Based Metal-Organic Framework Nanosheets on Ni Foam for High-Efficiency Electrochemical Water Splitting, *Catal. Lett.*, 2025, **155**, 1–10.
16 L. Zhao, et al., Construction of two-dimensional heterojunction to regulate metal d-band center of CoFe-MOF for efficient electrocatalytic water splitting, *J. Power Sources*, 2025, **641**, 236881.
17 R. Li, et al., Two-dimensional ultrathin donor-acceptor Co-based metal organic framework nanoplates for efficient electrocatalytic water splitting, *Int. J. Hydrogen Energy*, 2024, **79**, 998–1008.
18 H. He, et al., Recent advances in electrocatalysts for efficient hydrogen evolution reaction, *Rare Met.*, 2025, **44**, 2208–2238, DOI: 10.1007/s12598-024-02649-1.
19 D. K. Oh, et al., Study on catalyst-support interactions in high-entropy catalysts toward electrochemical water splitting reactions, *J. Am. Ceram. Soc.*, 2025, e70091.
20 L. Zhang, H. Wei, R. Yuan, P. Li and J. T. Ren, Interface engineering of transition-metal-based electrocatalysts for alkaline water splitting, *Coord. Chem. Rev.*, 2025, **545**, 217009.
21 C. Xu, et al., Transition metal-based heterojunctions for alkaline electrocatalytic water splitting, *Coord. Chem. Rev.*, 2025, **523**, 216287.
22 J. Chen, et al., Bifunctional Bimetal CoFe-MOF as Effective Electrocatalyst for the Water Splitting, *Catal. Lett.*, 2025, **155**, 231.
23 M. Moharramnejad, M. Babazadeh, A. Ehsani and S. M. Mahdian, MOF-derived carbon and transition metals as high efficient electrocatalysts and active materials in energy storage devices: an introduction and review to it in recent studies, *Inorg. Nano-Met. Chem.*, 2025, **55**, 273–306, DOI: 10.1080/24701556.2023.2267538.
24 M. R. Tamtam, R. Koutavarapu, R. Wang, G. S. Choi and J. Shim, Cobalt–copper MOF: a high-performance and ecofriendly electrode material for symmetric and asymmetric supercapacitors, *Mater. Sci. Semicond. Process.*, 2025, **188**, 109220.
25 Y. Xie, et al., Hollow transition metal chalcogenides derived from vanadium-based metal organic framework for hybrid supercapacitors with excellent energy-density and stability, *J. Colloid Interface Sci.*, 2025, **680**, 446–455.
26 C. Xiong and Y. Su, Recent Progress of Transition Metal-Based Oxide Composite Electrode Materials in Supercapacitor, *Adv. Sustainable Syst.*, 2025, **9**, 2400578.
27 G. L. Deolikar, P. Jain, A. Shrivastava and R. V. Motghare, Synergistic effects of Ni particles within Co-BDC MOF (Ni@Co-BDC) for high-performance supercapacitors, *Inorg. Chem. Commun.*, 2025, **175**, 114110.
28 H. Laeim, et al., Porosity Tunable Metal-Organic Framework (MOF)-Based Composites for Energy Storage Applications: Recent Progress, *Polymers*, 2025, **17**, DOI: 10.3390/polym17020130.
29 L. Zhang, Y. Wang, C. Yang and K. Tao, Metal-Organic Framework-Based Electrodes for Asymmetric Supercapacitors, *Batteries Supercaps*, 2025, **8**, e202400534.
30 Y. X. Lai, R. Y. Li and C. Young, High-Performance Mo-CoS_2 Nanoplates Derived from Metal-Organic Frameworks for Asymmetric Supercapacitor Applications, *ChemPhysChem*, 2025, **26**, 2400910.
31 M. A. Borysiewicz, J. H. Dou, I. Stassen and M. Dincă, Why conductivity is not always king-physical properties governing the capacitance of 2D metal-organic framework-based EDLC supercapacitor electrodes: a $Ni_3(HITP)_2$ case study, *Faraday Discuss.*, 2021, **231**, 298–304.
32 J. W. Gittins, et al., Insights into the electric double-layer capacitance of two-dimensional electrically conductive

metal-organic frameworks, *J. Mater. Chem. A*, 2021, **9**, 16006–16015.
33 L. Kang, S. X. Sun, L. B. Kong, J. W. Lang and Y. C. Luo, Investigating metal-organic framework as a new pseudocapacitive material for supercapacitors, *Chin. Chem. Lett.*, 2014, **25**, 957–961.
34 O. Kulkarni, et al., Dual redox center-based copper-cobalt metal–organic framework as pseudocapacitive electrode material for supercapacitor, *Inorg. Chem. Commun.*, 2025, **172**, 113711.
35 W. Shoukat, et al., Optimizing hybrid supercapacitor performance through synergistic integration of metal-organic frameworks and metal oxides, *RSC Adv.*, 2025, **15**, 25221–25232.
36 K. Sun, et al., In-situ growth strategy to design metal-organic frameworks separators for efficient Zn-ion hybrid supercapacitors, *Chem. Eng. J.*, 2025, **511**, 162004.
37 A. Kumar, et al., Bimetallic MOF-derived CuO-Co_3O_4 heterostructures as high-capacity electrodes for asymmetric supercapacitors, *Chem. Eng. J.*, 2025, **520**, 165685.
38 J. Zia and M. S. S. R. Tejaswini, Advancements in binary and ternary transition metal-based composites for high-performance supercapacitors: a comprehensive review, *RSC Adv.*, 2025, **15**, 9055–9080, DOI: **10.1039/d5ra00528k**.
39 F. Ran, et al., Designing transition metal-based porous architectures for supercapacitor electrodes: a review, *RSC Adv.*, 2024, **14**, 11482–11512, DOI: **10.1039/d4ra01320d**.
40 R. Nivetha, et al., Two-dimensional bimetallic Fe/M- (Ni, Zn, Co and Cu) metal organic framework as efficient and stable electrodes for overall water splitting and supercapacitor applications, *J. Energy Storage*, 2023, **61**, 106702.
41 J. H. Shah, et al., Redox active cobalt based bi-linker metal organic frameworks derived from 5-sulfoisopthalic acid and 4,4-bipyridine for supercapacitor, *Mater. Res. Bull.*, 2025, **181**, 113123.
42 J. Xing, et al., High-Entropy Metal–Organic Frameworks and Their Derivatives: Advances in Design, Synthesis, and Applications for Catalysis and Energy Storage, *Advanced Science*, 2025, **12**, 2411175.
43 K. Rashid, et al., Role of metal-organic frameworks (MOFs) in electrochemical energy storage devices including batteries and supercapacitors, *Rev. Inorg. Chem.*, 2025, DOI: **10.1515/revic-2024-0137**.
44 Y. Gao, G. Ji and Z. Fang, Microchemistry of 2D MOFs and their derivatives: from synthesis and catalytic mechanisms to energy storage, *J. Adv. Res.*, 2025, DOI: **10.1016/J.JARE.2025.06.073**.
45 B. Y. Guan, X. Y. Yu, H. B. Wu and X. W. D. Lou, Complex Nanostructures from Materials based on Metal–Organic Frameworks for Electrochemical Energy Storage and Conversion, *Adv. Mater.*, 2017, **29**, 1703614.
46 S. Anand and K. R. P. Sunajadevi, CuNi-PTC metal-organic framework: unveiling pseudocapacitive energy storage and water splitting capabilities, *Nanoscale Adv.*, 2025, **7**, 4129–4141.
47 T. Pan, et al., MOF-Based Electrocatalysts for Water Electrolysis, Energy Storage, and Sensing: Progress and Insights, *Chem. Rec.*, 2025, **25**, e202400253.
48 Y. Tang, H. Zhang, Y. Jin, J. Shi and R. Zou, Boosting the electrochemical energy storage and conversion performance by structural distortion in metal–organic frameworks, *Chem. Eng. J.*, 2022, **443**, 136269.
49 R. Du, et al., Porosity Engineering of MOF-Based Materials for Electrochemical Energy Storage, *Adv. Energy Mater.*, 2021, **11**, 2100154.
50 H. Chen, et al., Active Site Engineering in Porous Electrocatalysts, *Adv. Mater.*, 2020, **32**, 2002435.
51 J. Qi, W. Zhang and R. Cao, Porous Materials as Highly Efficient Electrocatalysts for the Oxygen Evolution Reaction, *ChemCatChem*, 2018, **10**, 1206–1220, DOI: **10.1002/cctc.201701637**.
52 C. Liu, X. Zhang, Y. Cheng, X. Hao and P. Yang, NiS/Ni_3S_4 decorated double-layered hollow carbon spheres for efficient electrochemical hydrogen evolution reaction and supercapacitor, *Electrochim. Acta*, 2024, **477**, 143751.
53 Y. Han, Z. Liu, C. Wang, L. Guo and Y. Wang, Construction of rod-like cobalt-pyridinedicarboxylic acid/MXene nanosheets composites for hydrogen evolution reaction and supercapacitor, *J. Colloid Interface Sci.*, 2024, **661**, 139–149.
54 A. U. Rehman, et al., MOF-Based Composite Materials for Supercapacitors: Design, Performance, and Challenges, *Chem.–Asian J.*, 2025, **20**, e00453.
55 D. Senthil Raja, X. F. Chuah and S. Y. Lu, In Situ Grown Bimetallic MOF-Based Composite as Highly Efficient Bifunctional Electrocatalyst for Overall Water Splitting with Ultrastability at High Current Densities, *Adv. Energy Mater.*, 2018, **8**, 1801065.
56 Q. Akbar Sial, et al., Synergistic Effect of Donor Doping on In-Situ Synthesized Co(M)-$NiSe_2$–VSe_2 for Battery-Type Supercapacitor and Oxygen Evolution Reaction Applications, *Chem. Eng. J.*, 2025, **503**, 158368.
57 J. Yang, et al., Synthesis of NiCoMn ternary metal–organic frameworks with a hollow spherical structure for high-performance asymmetric supercapacitors, *J. Mater. Sci.: Mater. Electron.*, 2023, **34**, 1796.
58 M. W. Khan, et al., Electrodeposited nickel-manganese terephthalic acid metal organic framework for hybrid battery and water splitting, *J. Alloys Compd.*, 2025, **1010**, 177245.
59 A. Gupta, et al., Cobalt metal–organic framework derived cobalt–nitrogen–carbon material for overall water splitting and supercapacitor, *Int. J. Hydrogen Energy*, 2023, **48**, 9551–9564.
60 J. Khan, A. Ahmed and A. A. Al-Kahtani, From design to efficiency: cobalt-based MOFs for efficient and stable electrocatalysis in hydrogen and oxygen evolution reactions, *RSC Adv.*, 2025, **15**, 8420–8429.
61 N. G. Balasubramaniyan, N. P. Singh Chauhan and P. Perumal, Rational design of nickel-cerium bimetallic MOF decorated on g-C_3N_4 nanosheets as bifunctional

electrocatalysts for water splitting, *J. Electroanal. Chem.*, 2025, **978**, 118899.

62 A. Makda, et al., Enhancing Supercapacitor Performance of NiCoMn-Layered Double Hydroxide with Ag–Citrate/Polyaniline Nanocomposites, *Energy Technol.*, 2024, **13**, 2401730.

63 S. M. Abdullah, et al., Tailoring NiCoCu layered double hydroxide with Ag-citrate/polyaniline/functionalized SWCNTs nanocomposites for supercapacitor applications, *RSC Adv.*, 2024, **14**, 14438–14451.

64 M. A. Deyab, Q. Mohsen and O. A. A. El-Shamy, Designing novel Bi-metallic MOFs with optimized Ni and Co ions ratios for enhanced supercapacitor performance, *J. Energy Storage*, 2025, **105**, 114777.

65 T. Shaikh, et al., Designing of bimetallic rGO@Co/Mn MOF and bioderived carbon as efficient electrodes for high-performance asymmetric supercapacitor, *J. Energy Storage*, 2025, **112**, 115545.

66 X. Jiang, *et al.*, Green Synthesis, Characterization and Thermal Investigation of Ni(II) and Cu(II) Complexes Constructed by Pyridine-2,6-Dicarboxylic Acid, *J. Chem. Soc. Pak.*, 2024, **46**, 29, **http://www.ccdc.cam.ac.uk/conts/retrieving.html**.

67 M. Ranjbar, M. A. Taher and A. Sam, Facile hydrothermal synthesis of manganese-metal organic framework nanostructures in the presence of various organic ligands for SO_2 and CO_2 gas adsorption, *J. Porous Mater.*, 2016, **23**, 375–380.

68 R. Zahid, M. R. Abdul Karim, F. S. Khan and M. A. Marwat, Elucidating the performance of hexamethylene tetra-amine interlinked bimetallic NiCo-MOF for efficient electrochemical hydrogen and oxygen evolution, *RSC Adv.*, 2024, **14**, 13837–13849.

69 R. Zahid,, *et al*, Catalytically Active Bimetallic Nickel–Cobalt MOF Linked Via Pyridine 2, 6-Dicarboxylate for Electrochemical Water Splitting Applications, *Arabian J. Sci. Eng.*, 2025, **50**, 6625–6637.

70 T. Van Phuc, et al., Highly active Ni/Co-metal organic framework bifunctional electrocatalyst for water splitting reaction, *Int. J. Hydrogen Energy*, 2022, **47**, 22787–22795.

71 T. Zhang, et al., MOF-derived Co(Ni)O_x species loading on two-dimensional cobalt phosphide: a Janus electrocatalyst toward efficient and stable overall water splitting, *Appl. Mater. Today*, 2023, **34**, 101912.

72 S. Dilpazir, et al., Laser annealed Mn-doped NiCo-MOF derived bifunctional metal-carbon nanocomposite for efficient water splitting, *J. Power Sources*, 2025, **652**, 237637.

73 S. A. Haider, et al., Bimetallic metal-organic frameworks as versatile electrocatalysts for water splitting in neutral and alkaline environments, *Fuel*, 2025, **397**, 135488.

74 S. Ramesh, et al., Nanoscale synthesis of nickel oxide@carboxy methyl cellulose@nitrogen doped carbon nanotubes supported metal organic frameworks ternary composite for use symmetric supercapacitor, *Int. J. Biol. Macromol.*, 2025, **318**, 144901.

75 H. Shabbir, et al., Synergistic effect of 3D porous tri-metallic MOF based electrode materials for highly stable asymmetric supercapacitors, *Mater. Sci. Semicond. Process.*, 2025, **186**, 109036.

76 Y. Wang, et al., Controllable preparation of nickel cobalt manganese ternary metal-organic frameworks for high-performance supercapacitor, *J. Energy Storage*, 2023, **58**, 106395.

77 G. Nagaraju, S. C. Sekhar, B. Ramulu and J. S. Yu, High-performance hybrid supercapacitors based on MOF-derived hollow ternary chalcogenides, *Energy Storage Mater.*, 2021, **35**, 750–760.

78 C. Kang, et al., Metal-organic framework derived hollow rod-like NiCoMn ternary metal sulfide for high-performance asymmetric supercapacitors, *Chem. Eng. J.*, 2022, **427**, 131003.

79 L. Zhao, F. Meng and W. Zhang, Fabrication of 3D micro-flower structure of ternary Ni-Co-Cu hydroxide based on Co-MOF for advanced asymmetric supercapacitors, *Electrochim. Acta*, 2023, **461**, 142656.

80 H. N. Abdelhamid, Bimetallic Metal–Organic Framework (MOF)–Derived NiO/CuO-Embedded Carbon for Supercapacitor, *Appl. Organomet. Chem.*, 2025, **39**, e70193.

81 M. Saeed, et al., Synergistic interplay of 1D bimetal Co-Ni-MOF@rGO for hybrid energy storage device, *Diamond Relat. Mater.*, 2025, **157**, 112496.

82 X. Y. Zhang, et al., Heterobimetallic cobalt-nickel 2D MOF nanosheet with a super large conjugated organic ligand for high-capacitance supercapacitors, *J. Alloys Compd.*, 2025, **1016**, 178918.

83 N. Kumar, P. Bhattacharya, A. Jana and S. Kumar, Synergism induced multifunctional electroactivity of Co-Ni bimetallic metal-organic frameworks towards oxygen evolution reaction and supercapacitors, *Inorg. Chem. Commun.*, 2025, **177**, 114445.

84 Y. Liang, et al., Nickel cobalt bimetallic metal-organic frameworks with a layer-and-channel structure for high-performance supercapacitors, *J. Energy Storage*, 2021, **33**, 102149.

85 X. Hu, et al., Hierarchical $CuCo_2O_4$@CoS-Cu/Co-MOF core-shell nanoflower derived from copper/cobalt bimetallic metal–organic frameworks for supercapacitors, *J. Colloid Interface Sci.*, 2021, **600**, 72–82.

86 A. Ahmed, *et al.*, Zincronized NiCo selenides coupled with polypyrrole: a synergistic route to high-energy asymmetric supercapacitors, *RSC Adv.*, 2025, **15**, 35573–35585.